

BAR-ILAN UNIVERSITY

**Sub-Attosecond X-Ray
Hong-Ou-Mandel Metrology**

Sergey Volkovich

Submitted in partial fulfillment of the requirements for the
Master's Degree in the Department of Physics,
Bar-Ilan University

This work was carried out under the supervision of

Prof. Sharon Shwartz

Department of Physics, Bar-Ilan University

Acknowledgement

I would like to express my gratitude to my supervisor Prof. Sharon Shwartz, for his guidance and our insightful discussions throughout my Master's work.

I would also like to thank the Physics Department at Bar-Ilan University, for deepening my understanding of nature and for the administrative assistance throughout my undergraduate and graduate studies.

Finally, I would like to thank my family and my friends, for all of their support through all these years.

Contents

Abstract.....	i
1. Introduction.....	1
2. Background.....	4
2.1. The Hong-Ou-Mandel Effect.....	4
2.2. Electromagnetic Field Quantization	7
2.3. X-Ray Biphotons Sources.....	10
2.4. X-Ray Interferometry.....	14
2.5. Photodetectors.....	17
3. Procedures.....	18
3.1. System Design	18
3.2. Device Modeling.....	19
3.3. Coincidence Count Rate Calculation	20
3.4. Simulations	21
4. Outcomes	22
4.1. System Design	22
4.2. Device Modeling.....	24
4.2.1. SPDC Source Model.....	24
4.2.2. Phase Shifter Model.....	27
4.2.3. Multilayer Optical Devices Model.....	28
4.2.4. Photodetectors Model	30
4.3. Coincidence Count Rate Calculation	31
4.3.1. SPDC Source Coincidence Count Rate	31
4.3.2. HOM System Output Ladder Operators	35
4.3.3. HOM System Second Order Correlation Function.....	37
4.3.4. HOM System Coincidence Count Rate	44
4.3.5. SPDC Source Probability Amplitude.....	46

4.4. Simulations	48
4.4.1. SPDC Source Simulation	48
4.4.2. Multilayer Optical Devices Simulation	50
4.4.3. HOM Interferometer Simulation.....	52
5. Discussion and Summary.....	53
6. Bibliography	56
Hebrew Abstract	8

Abstract

In this work, I present a new metrology technique that allows the measurement of sub-attosecond delays and sub-Angstrom optical path differences, by using the Hong-Ou-Mandel effect in the x-ray regime. I propose a realistic scheme for an optical system demonstrating the effect with x-rays, which is compatible with existing technologies. This is the first consideration of the quantum effect of x-ray Hong-Ou-Mandel and is an important step in the expansion of quantum optics into the x-ray regime. Furthermore, I anticipate that the scheme I describe in this work will lead to numerous novel applications for fundamental science and applicative research, and especially to quantum measurement techniques with ultra-high precision at x-ray wavelengths.

The Hong-Ou-Mandel effect is a quantum effect of interference between the wave functions of two indistinguishable photons, which enter simultaneously into two different input ports of a 50:50 beam splitter. As a consequence of their indistinguishability, the photons are always detected at the same output port of the beam splitter, and the coincidence measurement of the output ports is nullified, which is a classically unexpected result. When the optical path difference between the photons increases, they no longer reach the beam splitter simultaneously and become more distinguishable. This raises the probability of coincident detection, which reaches $\frac{1}{2}$ when they become completely distinguishable. Thus, the delay between the photons can be measured on extremely short time scales.

Extending the Hong-Ou-Mandel effect to the x-ray regime will open new and intriguing possibilities for the study of quantum physics by utilizing the advantages of the high energy of the x-ray photons. Examples for such advantages are the penetrability of x-rays relative to optical photons, the ability to modulate them to carry more information, and the availability of photon number resolving detectors, which demonstrate high detection efficiencies and negligible background noise. The main advantages of this measurement approach over the present-day techniques are the ultra-high precision and the relaxed requirements for the stability of the system and for the coherence of the source. Hence, it can overcome the hindrances of present-day technologies, enabling the measurements of effects and quantities that are out of their reach, and will be advantageous for the broad spectrum of scientific disciplines.

To demonstrate the effect, I start by designing the optical system schematically. The proposed system is comprised of a source for the generation of indistinguishable broadband x-ray photon pairs, based on spontaneous parametric down-conversion, and a multilayer-based

interferometer, which accommodates the relatively wide bandwidth. I proceed to model the optical devices mathematically, then I calculate analytically the coincidence count rate at the output of the system, and finally I simulate an example system using Mathematica, for parameters which fit the design goals and reflect realistic device properties. The full width half max of the coincidence count rate versus the delay between the biphotons is found to be about 0.6 attoseconds. This highlights the capability of this metrology technique to measure sub-attosecond time delays and sub-Angstrom optical path differences.

1. Introduction

Since its first observation [1], the Hong-Ou-Mandel (HOM) effect has attracted a great attention due to its importance for fundamental quantum sciences and since it holds a great promise for new quantum technologies [2–16]. The HOM effect is a quantum effect that is based on the interference of the wave functions of the photons rather than on the interference of classical waves. The striking consequence of this quantum interference is manifested when two indistinguishable photons arrive simultaneously at the two different input ports of an ideal beam splitter. In contrast to classical waves, the two photons will always be detected at the same output port of the beam splitter. As a result, coincidence measurements of the output port are null as long as the photons at the two input ports are indistinguishable.

In a typical HOM experiment two indistinguishable photons are generated and propagate along two paths. By varying one of the optical paths, it is possible to control the delay between the two photons so that they do not arrive at the beam splitter simultaneously and their distinguishability is raised. The more distinguished the photons become, the higher the probability of coincident detection gets, until it reaches $\frac{1}{2}$ at complete distinguishability. This behavior can be used to measure the delay between the arrival times of the photons.

The ability of the HOM effect to detect the indistinguishability of photons on very short time scales has led to development of various approaches based on the effect for the measurements of ultrashort delays and optical path differences [17–20]. Measurements based on the HOM effect are more sustainable than measurements with classical interferometers, because unlike classical interferometers, HOM measurements are independent of the phase fluctuations of the optical beams. Consequently, in recent years several schemes and approaches for sub-femtosecond delay measurements with optical beams have been suggested and implemented [18,19].

Generally speaking, the extension of quantum optics itself to the x-ray regime can provide new intriguing opportunities. This is due to the availability of photon number resolving detectors with higher detection efficiencies and negligible signal to noise ratios, made possible by the relatively high photon energies. In addition, in many cases the photons are more penetrative than optical photons, and as they possess higher frequencies, they can be modulated to carry more information.

Several works on quantum effects in the x-ray regime have been reported in the past few years [21]. For example, the necessity of a full quantum theory to describe SPDC in the x-ray regime has been demonstrated in [22], quantum effects such as electromagnetically induced

transparency [23], collective Lamb shift [24], modulation of single γ photons [25], ghost imaging [26], quantum enhanced detection [27], and vacuum-assisted generation of atomic coherences [28] have been reported as well. In addition, several schemes for the generation of x-ray polarization entangled photons have been proposed [29–31].

To reap the benefits of extending the HOM effect to the x-ray regime, a key requirement is a source that can produce indistinguishable photon pairs (also known as biphotons). One prominent candidate source is spontaneous parametric down conversion (SPDC). In this type of source, a pump interacts with the vacuum field in a nonlinear crystal and indistinguishable biphotons can be generated [32]. Indeed, the keV wide bandwidth that has been reported for x-ray SPDC [22,33] suggests that the corresponding biphoton correlation time is on the order of a few attoseconds, which opens the possibility to measure delays that are on that order or even shorter, by using advanced approaches such as the Fisher information analysis [19,20]. In addition, the implementation of the x-ray HOM effect can lead to the development of quantum optical coherence tomography, for measurements of very short spatial scales and tiny refractive index differences at an unprecedented precision [34–37]. This would be appealing for the imaging of biological samples.

However, the possibility to measure such a broad spectrum HOM effect is not clear. The main challenge is that x-ray mirrors and beam splitters rely either on small angle reflection or on Bragg scattering [38,39]. Small angle reflection can be used to reflect a very broad spectrum, but the generated photons propagate in an angular cone, which is much broader than the acceptance angle of small angle reflection devices. Bragg scattering from crystals is narrow in both angle and spectrum, thus with crystal mirrors and beam splitter the HOM effect would be narrowband and the corresponding dip of the coincidence count rate would be limited to an order of a few femtoseconds. The alternative possibility is to use Bragg scattering from artificial periodic structures made by multilayers. However, it is not clear whether the technical feasibility of the present-day multilayer technology allows the fabrication of such a system. It is also not clear a priori that the photons that hit upon the two ports of the beam splitter are indeed indistinguishable, which is an essential requirement for the observation of the HOM effect.

In this work I describe a system that is based on available technologies for measuring the HOM effect at x-ray wavelengths, which consists of a nonlinear crystal for the generation of biphotons, a phase shifter, two multilayer mirrors, and a multilayer beam splitter. I show that the photons that hit the beam splitter are indeed indistinguishable when arriving simultaneously and that the system can support the detection of very short delays. I consider a specific example

where the full width half max (FWHM) of the dip is about 0.6 attoseconds and explain how to control this width. Consequently, my work indicates on the possibility for the development of systems that are capable to measure sub-attosecond time delays and sub-Angstrom optical path differences.

2. Background

In this section I present the background regarding the HOM effect and the physical entities composing the HOM system. I start by describing and explaining the HOM effect and then I describe the models that I use to represent each of the physical entities participating in the effect, which are the electromagnetic field, the biphotons source, the interferometer and the photodetectors.

2.1. The Hong-Ou-Mandel Effect

The HOM effect is a quantum optical effect of interference between the wave functions of an indistinguishable photon pair, in which the two photons enter different input ports of a 50:50 beam splitter. As a result of this setup, the exiting photons are always detected at the same output port of the beam splitter [1,32]. The system demonstrating the effect can be seen in Fig. 1.

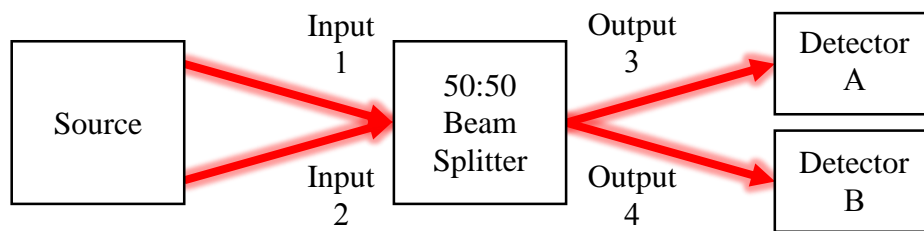


FIG. 1. Schematic diagram of the Hong-Ou-Mandel effect system. Two indistinguishable photons are generated from a source, arrive at the two different input ports of a 50:50 beam splitter (Input 1 and Input 2), and are detected by two detectors, each positioned at one of the two different output ports of the beam splitter (Output 3 and Output 4).

To understand the effect, consider an ideal beam splitter, whose input ports will be marked by “1” and “2” and output ports will be marked by “3” and “4”. Classically, the energy of the radiation is expected to split between the output ports of the beam splitter, being detectable at both of them simultaneously. In contrast, when considering the quantization of radiation, each photon can only either reflect or transmit, which creates four output combinations. As we will see next, the indistinguishability of the biphotons causes only two outcomes to be possible, those where both photons exit the same port. Therefore, the number of coincidence counts between the outputs is nullified, and measuring it exhibits the non-classical behavior of the electromagnetic radiation.

This can be described mathematically by modelling the beam splitter by a unitary transformation, relating the input and output creation operators. As an example, I shall choose:

$$\begin{pmatrix} \hat{a}_1^\dagger \\ \hat{a}_2^\dagger \end{pmatrix} = \frac{1}{\sqrt{2}} \begin{pmatrix} 1 & 1 \\ 1 & -1 \end{pmatrix} \begin{pmatrix} \hat{a}_3^\dagger \\ \hat{a}_4^\dagger \end{pmatrix}, \quad (2.1.1)$$

where \hat{a}_i^\dagger is a photon creation operator at port " i ". Every photon enters a different input port, so for single mode photons the input state can be described by:

$$|\psi\rangle_{in} = |1\rangle_1 |1\rangle_2, \quad (2.1.2)$$

where $|n\rangle_i$ is a Fock state representing " n " photons at port " i ". The output state is then calculated to be:

$$|\psi\rangle_{out} = \frac{1}{\sqrt{2}} (|2\rangle_3 |0\rangle_4 - |0\rangle_3 |2\rangle_4), \quad (2.1.3)$$

which shows that the exiting photons are always detected at the same port. Therefore, the coincidence count rate between both output ports drops to zero, which is a purely quantum result. We see that the intensity correlation is the quantity of interest.

As the distinguishability of the biphotons raises, the probability of coincident detection as a function of the distinguishability begins to raise from zero, until it reaches $\frac{1}{2}$ at complete distinguishability. When considering multimode photons, which possess a temporal distribution, the biphotons can be distinguished by their time of arrival to the beam splitter. This distinguishability can be varied by changing the optical path difference between the biphotons, thus creating a relative delay between them. In the private case in which the biphotons possess equal distributions, they become completely distinguishable when the delay between them reaches the width of their probability density function in the time domain.

The behavior of the number of coincidence counts when the distinguishability between the biphotons is changed can be seen in Fig. 2, which is taken from the original paper [1]. In the original experiment the delay between the biphotons was modified by changing the position of the beam splitter. When the beam splitter is positioned such that the relative delay nullifies and the biphotons are indistinguishable, the number of coincidence counts dips towards zero. The width of the dip is comparable to the width of the biphoton probability density function in the time domain, or, equivalently, to the inverse of its width in the frequency domain.

The time interval between the biphotons was measured to be as short as approximately 100 fs, and I will show that in my proposed system this interval decreases to attoseconds. This occurs since in my system the bandwidth that reaches the beam splitter was designed to be wider than the bandwidth in the original experiment by over 5 orders of magnitude.

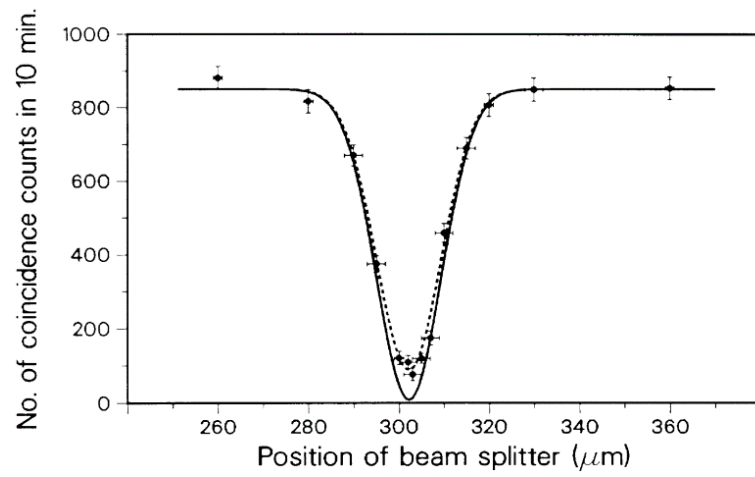


FIG. 2. The measured (dotted line) and theoretical (solid line) number of coincidence counts in ten minutes as a function of the displacement of the beam splitter in the original paper. The vertical error bars correspond to a standard deviation and the horizontal are based on measurement accuracy estimates.

2.2. Electromagnetic Field Quantization

This work utilizes a quantum model of the electromagnetic field which is obtained by a different procedure than the one commonly used in quantum optics. In this model, the number operator represents the number of energy flux (intensity) quanta in a field mode instead of energy quanta. The motivation behind this is that the energy flux is the conserved physical quantity in optical processes according to Poynting theorem. This fact holds quantum mechanically as well, and in particular, at the source of the system, the quantity that is converted from the pump field to the signal and idler fields is a quantum of energy flux. In addition, the energy flux is what is measured in practice, and this model is also justified experimentally and has been used by parts of the quantum optics community for years, including our group [22,26,27,33]. Another justification is that it allows to find equations similar to the Heisenberg equation for the ladder operators, in which a position derivative appears instead of the time derivative, but position and time are related through the speed of light, c . Overall, it has become significantly more probable that this model describes reality better than the alternatives.

Also, while it is common to neglect the spatial dependence of the ladder operators in quantum optics, this work utilizes the general model in which the spatial dependence is included. This allows to calculate the full spatiotemporal dependence of the physical quantities of interest.

The quantization of the electromagnetic field is achieved by the following procedure. The classical electric field modes of a physical system of interest are specified. Then, an operator is defined to represent the field dynamical variable from the classical physical quantity. Finally, the operator is expressed via ladder operators and the corresponding bosonic commutation relations are set. The ladder operators are defined based on the electric field, instead of the commonly used vector potential, by comparing the number operator to the intensity of a field mode. This causes the ladder operators to have the physical meaning of creating or destroying one quantum of energy flux, instead of a quantum of energy, and the resulting discretized physical quantity becomes the energy flux.

In this work, the quantization procedure is performed for the following general classical electric field modes, which are expected on physical grounds. The modes are monochromatic plane waves with varying amplitudes and a continuous frequency range:

$$\vec{E}(x, y, z, t) = E(x, y, z, t)e^{i(\vec{k}\cdot\vec{r}-\omega t)}\hat{e} + c. c., \quad (2.2.1)$$

where E is the complex amplitude of the monochromatic plane wave, \vec{k} is its wavevector, ω is its angular frequency, and \hat{e} is its polarization.

Looking at the intensity of the field and comparing it to the intensity operator allows to find the relation between the electric field and the ladder operators. The intensity of a field mode is:

$$I = \frac{EE^*}{2\eta} \cos(\theta), \quad (2.2.2)$$

where η is the impedance of the wave and θ its propagation angle, which effects the intensity.

Comparing this expression to the intensity in terms of the number operator:

$$\hat{I} = \hbar\omega \hat{a}^\dagger \hat{a}, \quad (2.2.3)$$

leads to the following substitution:

$$E_j \rightarrow \left(\frac{2\eta_j \hbar\omega_j}{\cos(\theta_j)} \right)^{0.5} \hat{a}_j. \quad (2.2.4)$$

It is immediately noticeable that the ladder operators are not unitless in this framework. The physical meaning of the operators \hat{a}_j and \hat{a}_j^\dagger when they act on the vacuum state is of destroying or creating a quantum of energy flux in a mode j , respectively, and they possess the following units:

$$[\hat{a}_j] = \frac{1}{m \cdot s^{0.5}}. \quad (2.2.5)$$

The number operator, $\hat{a}_j^\dagger \hat{a}_j$, has the meaning of representing the measurement of the number of detected quanta of energy flux in mode j . Its units are of flux:

$$[\hat{a}_j^\dagger \hat{a}_j] = \frac{1}{m^2 \cdot s}. \quad (2.2.6)$$

Additionally, similar to the field amplitudes, the ladder operators depend on space and time, or the corresponding frequency domain variables. For an example, the notation $\hat{a}_j(k_x, k_y, k_z, \omega)$ denotes a destruction operator of a quantum of flux in mode (k_x, k_y, k_z, ω) , with j further specifying the field mode.

To relate the real and frequency domains, the following definition of the Fourier transform is used:

$$F(z, \vec{q}, \omega) = \frac{1}{(2\pi)^3} \int_{-\infty}^{\infty} \int_{-\infty}^{\infty} f(z, \vec{r}, t) e^{i\vec{q} \cdot \vec{r}} e^{-i\omega t} d\vec{r} dt, \quad (2.2.7)$$

$$f(z, \vec{r}, t) = \int_{-\infty}^{\infty} \int_{-\infty}^{\infty} F(z, \vec{q}, \omega) e^{-i\vec{q} \cdot \vec{r}} e^{i\omega t} d\vec{q} d\omega,$$

where $\vec{r} \equiv (x, y)$ and $\vec{q} \equiv (k_x, k_y)$.

Thus, for the ladder operators:

$$\begin{aligned}\hat{a}_j(z, \vec{q}, \omega) &= \frac{1}{(2\pi)^3} \int_{-\infty}^{\infty} \int_{-\infty}^{\infty} \hat{a}_j(z, \vec{r}, t) e^{i(\vec{q}\cdot\vec{r}-\omega t)} d\vec{r} dt, \\ \hat{a}_j(z, \vec{r}, t) &= \int_{-\infty}^{\infty} \int_{-\infty}^{\infty} \hat{a}_j(z, \vec{q}, \omega) e^{-i(\vec{q}\cdot\vec{r}-\omega t)} d\vec{q} d\omega.\end{aligned}\tag{2.2.8}$$

Throughout the work, the Fourier transforms are only performed on the time domain variables x, y and t , which transform to k_x, k_y and ω , respectively. That is because the z axis acts as the optical axis and no momentum conservations are related to it in the analysis of the photon source of the system. I note that the following useful expressions for the Dirac delta function follow from the Fourier transform:

$$\delta(\vec{r}) = \left(\frac{1}{2\pi}\right)^2 \int_{-\infty}^{\infty} e^{-i\vec{q}\cdot\vec{r}} d\vec{q}, \quad \delta(t) = \frac{1}{2\pi} \int_{-\infty}^{\infty} e^{i\omega t} d\omega.\tag{2.2.9}$$

The commutation relations between the ladder operators in the frequency domain are set to be [22]:

$$\begin{aligned}& [\hat{a}_j(z_1, \vec{q}_1, \omega_1), \hat{a}_k^\dagger(z_2, \vec{q}_2, \omega_2)] \\ &= \frac{1}{(2\pi)^3} \delta_{j,k} \delta(z_1 - z_2) \delta(\vec{q}_1 - \vec{q}_2) \delta(\omega_1 - \omega_2).\end{aligned}\tag{2.2.10}$$

The corresponding commutation relations in the time domain are:

$$[\hat{a}_j(z_1, \vec{r}_1, t_1), \hat{a}_k^\dagger(z_2, \vec{r}_2, t_2)] = \delta_{j,k} \delta(z_1 - z_2) \delta(\vec{r}_1 - \vec{r}_2) \delta(t_1 - t_2).\tag{2.2.11}$$

To describe how the wave functions and the operators change throughout an optical system, the Heisenberg picture is used. In this picture, the operators are considered to evolve along the system, while the wave function remains unchanged. Thus, when calculating expectation values at a location of interest, the operators are plugged in after their propagation to the location along with the wave function at the input of the system. A useful result derived from the above is the vacuum expectation values of frequency domain operators at the same z :

$$\begin{aligned}\langle 0 | \hat{a}_j(\vec{q}_1, \omega_1) \hat{a}_k^\dagger(\vec{q}_2, \omega_2) | 0 \rangle &= \frac{1}{(2\pi)^3} \delta_{j,k} \delta(\vec{q}_1 - \vec{q}_2) \delta(\omega_1 - \omega_2), \\ \langle 0 | \hat{a}_j^\dagger(\vec{q}_1, \omega_1) \hat{a}_k(\vec{q}_2, \omega_2) | 0 \rangle &= 0, \\ \langle 0 | \hat{a}_j^\dagger(\vec{q}_1, \omega_1) \hat{a}_k^\dagger(\vec{q}_2, \omega_2) | 0 \rangle &= 0, \\ \langle 0 | \hat{a}_j(\vec{q}_1, \omega_1) \hat{a}_k(\vec{q}_2, \omega_2) | 0 \rangle &= 0,\end{aligned}\tag{2.2.12}$$

where $\delta_{j,k}$ is the Kronecker delta. To use this to calculate expectation values at a desired point, the operators at that location must be expressed via the operators at the input of the system, so that they will have the same z as the operators inside the expression of the wave function.

2.3. X-Ray Biphotons Sources

Predominant sources used to generate indistinguishable photon pairs for experiments are the process of spontaneous parametric down-conversion (SPDC) [32], atomic cascades and quantum dots [8]. The latter is not available at x-ray wavelengths yet and will not be easy to control. SPDC is a second order nonlinear process in which a photon interacts with the vacuum field via a medium and is converted into two photons while energy and momentum are conserved [32]. X-ray SPDC was proposed by Freund and Levine in 1969 [40] and observed by a number of groups since 1971 [41], including ours [22,33].

Being a second order nonlinear process, SPDC involves two frequencies that combine to create a third frequency. It originates from the interactions between a pump photon at frequency ω_p and the vacuum field fluctuations via a nonlinear medium. The interaction causes the pump photon to be converted into two photons, denoted as the “signal” and the “idler”, at lower frequencies ω_s and ω_i , respectively. The process is parametric thus energy is conserved in the form:

$$\hbar\omega_p = \hbar\omega_s + \hbar\omega_i. \quad (2.3.1)$$

To obtain an efficient process in nonlinear optics the energy should be transferred optimally from the pump to the desired generated fields. This can be done by maintaining the momentum conservation, a condition called “phase matching”:

$$\vec{k}_p = \vec{k}_s + \vec{k}_i. \quad (2.3.2)$$

Here \vec{k}_p , \vec{k}_s , and \vec{k}_i are the wave vectors of the pump, signal, and idler, respectively. To maintain the phase matching equation for a selected nonlinear process, specific refractive indices are used for the waves, through material choices. Since refractive indices for x-rays are near unity [38], it is not sufficient to use them for phase matching. Instead the reciprocal lattice vectors are used as proposed by Freund and Levine [40], which is possible since the wave vectors have the same order of magnitude. The phase matching equation becomes:

$$\vec{k}_p + \vec{G}(hkl) = \vec{k}_s + \vec{k}_i, \quad (2.3.3)$$

where $\vec{G}(hkl)$ is the reciprocal lattice vector corresponding to the Miller indices h , k , and l .

In the x-ray region, the interactions with the medium can be described classically by using a free electron gas model for the electrons [40,41], which is justified since the energy of the photons is much greater than the ionization energy of the electrons. The equations of motion and continuity are:

$$\frac{\partial \vec{v}}{\partial t} + (\vec{v} \cdot \nabla) \vec{v} = -\frac{e}{m} (\vec{E} + \vec{v} \times \vec{B}), \quad (2.3.4)$$

$$\frac{\partial \rho}{\partial t} + \nabla \cdot (\rho \vec{v}) = 0, \quad (2.3.5)$$

where \vec{E} is the electric field, \vec{B} is the magnetic field, e and m are the electron charge and mass, respectively, \vec{v} is the velocity of the electron and ρ is its charge density. The nonlinearity has contributions from three processes: the spatial variation of the velocity, the Lorentz Force and the spatial modulation of the charge density.

By using the perturbation theory for the free electron gas model, the envelope of the nonlinear current density is found to be [29]:

$$J_s^{NL} = -\frac{e^2 \rho_g \omega_s E_p E_i^*}{4m^2 \omega_p^2 \omega_i^2 \omega_s^2} \quad (2.3.6)$$

$$\times [\omega_i \omega_p (\vec{G} \cdot \hat{e}_s)(\hat{e}_p \cdot \hat{e}_i) - \omega_s \omega_i (\vec{G} \cdot \hat{e}_p)(\hat{e}_i \cdot \hat{e}_s) + \omega_s \omega_p (\vec{G} \cdot \hat{e}_i)(\hat{e}_p \cdot \hat{e}_s)].$$

Here E_p and E_i are the amplitudes of the pump and idler, respectively, $\hat{e}_p, \hat{e}_s,$ and \hat{e}_i are the polarization unit vectors of the pump, signal, and idler, respectively, and ρ_g is the Fourier component of the charge density for the corresponding reciprocal lattice vector. When the angle between the pump and the signal and idler is approximately straight, the second term in the nonlinear current density becomes the dominant term and the expression becomes:

$$J_s^{NL} = \frac{e^2 \rho_g E_p E_i^*}{4m^2 \omega_p^2 \omega_i} (\vec{G} \cdot \hat{e}_p)(\hat{e}_i \cdot \hat{e}_s). \quad (2.3.7)$$

For the term to not nullify, we see that the pump polarization must be inside the scattering plane, since \vec{G} is in the scattering plane.

By choosing a pump polarization inside the scattering plane and a nearly straight angle between the pump and both biphotons, as suggested by Borodin et al. in [33], the background noise caused by Bragg and Compton scattering is suppressed. This occurs since for photon energies above the electron binding energies, the cross section of these scattering processes is approximately the Thomson cross section, which approaches zero when viewed in the mentioned conditions. This choice requires the biphotons to be nearly parallel, and together with the choice of having identical biphoton frequencies, the solution of the phase matching condition is that the biphotons are very close to the Bragg angle. This poses no problem as Bragg scattering is suppressed, as mentioned.

Another useful result is that when transmission (Laue) geometry is used, a relative improvement of over an order of magnitude in the SNR is achieved [22]. The overall setup of the nonlinear crystal under the mentioned conditions can be seen in Fig. 3, where the z axis is set in the direction parallel to the lattice planes.

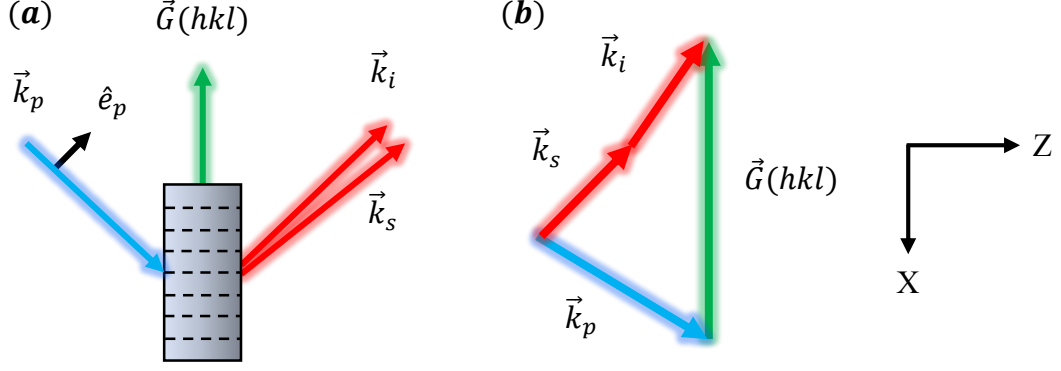


FIG. 3. (a) Schematic diagram of the nonlinear crystal in transmission geometry. \vec{k}_p , \vec{k}_s , and \vec{k}_i are the wave vectors of the pump, signal, and idler, respectively, $\vec{G}(hkl)$ is the reciprocal lattice vector corresponding to the Miller indices h , k , and l , which is orthogonal to the lattice planes represented by the dashed lines. The polarization unit vector of the pump, \hat{e}_p , is inside the scattering plane, and the angle between the pump and the generated biphotons is approximately straight. (b) The phase matching scheme.

The radiation propagating through the nonlinear crystal is described classically by Maxwell's equations and a wave equation is required for each of the pump, signal and idler frequencies. Each equation is Fourier transformed from (z, x, y, t) to (z, k_x, k_y, ω) , and the source term of these inhomogeneous equations, representing the nonlinearity, is the previously found nonlinear current density.

Since SPDC is a very inefficient process, the “undepleted pump approximation” is assumed, which states that the pump field remains constant and removes the need in the pump equation. Losses are inherent to x-ray wavelengths, but the loss terms were neglected on account of the materials being shorter than the absorption length for the parameters in this work. The “slowly varying envelope approximation” is also assumed, which applies when the envelope of a wave varies slowly in time and space compared to the wavelength and allows neglecting successive derivatives. For example:

$$\left| \frac{\partial^2 E}{\partial x^2} \right| \ll \left| k_x \frac{\partial E}{\partial x} \right|, \quad \left| \frac{\partial^2 E}{\partial z^2} \right| \ll \left| k_z \frac{\partial E}{\partial z} \right|, \quad \left| \frac{\partial J}{\partial t} \right| \ll |\omega J|. \quad (2.3.8)$$

Next, the wave equations are quantized to obtain a quantum description in the Heisenberg picture, by substituting the field envelope with a ladder operator. Their commutation relations in the frequency domain are given by [22]:

$$[\hat{a}_j(z_1, \vec{q}_1, \omega_1), \hat{a}_k^\dagger(z_2, \vec{q}_2, \omega_2)] \quad (2.3.9)$$

$$= \frac{1}{(2\pi)^3} \delta_{j,k} \delta(z_1 - z_2) \cdot \delta(\vec{q}_1 - \vec{q}_2) \delta(\omega_1 - \omega_2),$$

with $\vec{q} \equiv (k_x, k_y)$, and the relation between the real and frequency domain ladder operators is:

$$\hat{a}_j(z, \vec{r}, t) = \int_{-\infty}^{\infty} \int_{-\infty}^{\infty} \hat{a}_j(z, \vec{q}, \omega) e^{-i(\vec{q} \cdot \vec{r} - \omega t)} d\vec{q} d\omega. \quad (2.3.10)$$

Consequently, the generation of the biphotons in the nonlinear crystal is described by the following frequency domain coupled equations for the signal and idler envelope ladder operators in the Heisenberg picture for a lossless medium [22,33]:

$$\begin{cases} \frac{\partial \hat{a}_s}{\partial z} = \kappa \hat{a}_i^\dagger e^{i\Delta k_z z} \\ \frac{\partial \hat{a}_i^\dagger}{\partial z} = \kappa^* \hat{a}_s e^{-i\Delta k_z z} \end{cases}. \quad (2.3.11)$$

Here κ is a coupling coefficient and Δk_z is the phase mismatch in the z direction: $\Delta k_z = k_p \cos(\theta_p) - k_s \cos(\theta_s) - k_i \cos(\theta_i)$. θ_p , θ_s , and θ_i are the angles between the lattice plane and the wave vector of the pump, signal, and idler, respectively.

2.4. X-Ray Interferometry

X-rays are challenging to manipulate, as their refractive indices are roughly equal to one [38], which causes them to stay in nearly the same direction when they enter media. The refractive indices are commonly notated as:

$$n(\omega) = 1 - \delta(\omega) + i\beta(\omega), \quad (2.4.1)$$

with $\delta, \beta \ll 1$. The absorption length in this regime in terms of the above quantities is given by:

$$l_{\text{absorption}} = \frac{\lambda}{4\pi\beta}. \quad (2.4.2)$$

This quantity can achieve relatively small values, for example 150 μm for silicon at a photon energy of 10.5 keV, which also poses a challenge and must be considered when designing optical devices.

Interferometry between the x-ray photon pairs can be performed with different setups and types of devices, where the three commonly used mechanisms are total external reflection, Bragg devices made of single crystals and multilayer devices [38,39].

Since their refractive index is smaller than one, when x-rays are incident on materials from the vacuum, they experience total external reflection at incidence angles below a critical angle:

$$\theta_c = \sqrt{2\delta}, \quad (2.4.3)$$

where the angle is measured from the interface. Unfortunately, these angles are very small, for example 0.17 degrees for silicon at a photon energy of 10.5 keV. This limits greatly the required angles of the generated biphotons and the entrance angles of the other devices, which are not always available, making the mechanism less useful for our goal relative to the other two.

Bragg devices are based on the ability to utilize Bragg diffraction in this regime. Their downside is their relatively narrow bandwidths, for an example of several eVs for silicon at the lowest allowed reflection, while the bandwidths of SPDC photons reach an order of magnitude of several keVs. This lowers the coincidence count rate and narrows the dip curve. An additional issue is the inability to design devices for every photon energy and direction combination easily, and usually at all. Especially, it is impossible to find scattering planes for very small angles such as the ones arising when working with nearly collinear biphotons. Both of these issues are overcome by using multilayers [38].

Multilayer devices are composed of alternating layers of two materials with different refractive indices, which are deposited on a substrate. Scattering occurs at the boundary between every two layers due to the variation in the density of the scatterers. To maximize the

variation, a material with a high atomic number and a material with a low atomic number are chosen. These are commonly referred to as the “absorber” and “spacer”, respectively, and their widths are indicated by d_a and d_s . A ratio factor is defined as $\Gamma \equiv d_a/d$, with d being the width of the bilayers. The refractive indices and material lengths can be tailored to achieve adjustable optical properties, such as a specific reflectivity and transmission for desired photon energies and incidence angles, creating nearly ideal 50:50 beam splitters and mirrors. A schematic diagram of a multilayer device can be seen in Fig. 4:

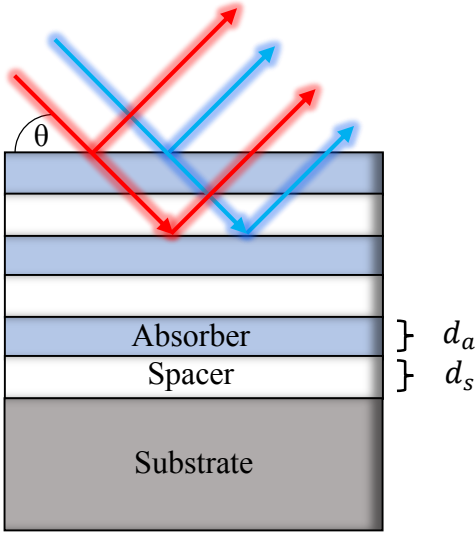


FIG. 4. Schematic diagram of a multilayer device. The device is composed of alternating layers of a material with a high atomic number and a material with a low atomic number, denoted as the “absorber” and the “spacer”, respectively, which are deposited on a substrate. θ is the angle of incidence, and d_a and d_s are the widths of the absorber and spacer layers, respectively.

Radiation with wavelength λ can be diverted by the system by attaining constructive interference between the waves reflected from the bilayers. Similar to Bragg diffraction, constructive interference occurs when the phase difference acquired between consecutive bilayers is equal to an integer multiple of the wavelength [38]:

$$2d \sin(\theta) = m\lambda, \quad (2.4.4)$$

where θ is measured from the surface, and m is a positive integer.

A more precise condition for constructive interference can be found by taking into account the refraction that occurs when the radiation propagates between the layers [39]:

$$2d \sin(\theta) \sqrt{1 - 2 \frac{\Gamma \delta_a + (1 - \Gamma) \delta_s}{\sin^2(\theta)}} = m\lambda. \quad (2.4.5)$$

Here $1 - \delta_a$ and $1 - \delta_s$ are the real parts of the refractive indices of the absorber and the spacer, respectively. This formula can be used to find the necessary width of the bilayers for a specific wavelength and incidence angle.

By using the recursive theory of multilayers [42], an analytical expression for the intensity reflectivity of N bilayers can be obtained, where the incident angle is equal to the Bragg angle and the refractions and the reflections from the substrate are negligible [39]:

$$R = \tanh^2[2Nrsin(\pi m\Gamma)]. \quad (2.4.6)$$

Here r is the amplitude reflectivity of the interface between the absorber and the spacer. From this expression, the required number of bilayers for 100% and 50% reflectivity can be calculated, which allows creating an ideal mirror and beam splitter. Notice that the intensity reflectivity is maximal when $m\Gamma$ is a semi-integer. Also, notice that this formula only provides the reflectivity for a specific wavelength at a specific angle, while SPDC photons contain many frequencies and angles.

For given multilayer parameters, the reflectivity and the transmission of a device as a function of the photon frequency and incidence angle can be found by a numerical calculation, based on the multilayer matrix theory approach [43]. Every device is divided into a stack of adjacent subsystems, such as layers and boundaries, and every subsystem is described by a transfer matrix relating the complex wave amplitudes at both of its sides. The individual matrices are then multiplied to find the total transfer matrix of the entire stack. A quantum transfer matrix can be obtained from the classical one by means of the quantization procedure described earlier.

2.5. Photodetectors

Photons can be detected via the photoelectric effect, wherein photons incident on a material ionize its electrons if their energies are higher than the binding energies of the electrons. The released photoelectrons can then be amplified and detected. Due to the relatively high energies of x-ray photons, single photon counters have very low noise and high quantum efficiency, which is advantageous for quantum optics.

In order to demonstrate the HOM effect, the detection of interest is the measurement of the coincidence count rate between the two output ports of the beam splitter. To calculate it analytically for a given optical system, it is useful to first calculate the second order correlation function. Then the second order correlation function can be integrated over the parameters of the detectors to obtain the rate.

Following the photodetection theory of Glauber [44], the second order correlation function in the framework of this work is given by:

$$G^{(2)}(\vec{r}_1, t_1, \vec{r}_2, t_2) = \langle \Psi | \hat{a}_Y^\dagger(\vec{r}_2, t_2) \hat{a}_X^\dagger(\vec{r}_1, t_1) \hat{a}_X(\vec{r}_1, t_1) \hat{a}_Y(\vec{r}_2, t_2) | \Psi \rangle. \quad (2.5.1)$$

Here the subscripts "X" and "Y" denote two different detectors, which are positioned at the two different outputs of the final device in the system, $\vec{r} = (x, y)$, and the detectors are assumed to be at the same z , so the z -dependence is not written explicitly. It has the physical meaning of the flux of detecting one photon at detector X at (\vec{r}_1, t_1) , while detecting one photon at detector Y at (\vec{r}_2, t_2) . Its units are therefore the units of flux squared:

$$[G^{(2)}(\vec{r}_1, t_1, \vec{r}_2, t_2)] = \frac{1}{m^4 \cdot s^2}. \quad (2.5.2)$$

By integrating $G^{(2)}$ over the area of a detector and its detection window, the rate of detecting coincident photons at two detectors can be calculated. The coincidence count rate for two detectors is given by:

$$R_C = S \int \int G^{(2)}(\vec{r}_1, t_1, \vec{r}_2, t_2) d\vec{u} d\tau, \quad (2.5.3)$$

where S is the area of the input beam on the source crystal which generates the two photons, $\vec{u} = \vec{r}_2 - \vec{r}_1$ is the distance between the detection points, and $\tau = t_2 - t_1$ is the duration between the detections. Its units are of rate:

$$[R_C] = \frac{1}{s}. \quad (2.5.4)$$

3. Procedures

In this section I present the steps I have taken in order to design an optical system that demonstrates the HOM effect and to show that sub-attosecond delays and sub-Angstrom optical path differences can be measured with it. The steps can be divided into four stages: designing the system schematically, modeling the devices, calculating the coincidence count rate at the outputs of the source and of the entire system and simulating the devices and the entire system for example parameters using Mathematica.

3.1. System Design

In the first stage, I design the optical system schematically. This is done by selecting the optical devices comprising the system, while only considering their general function and disregarding their specific parameters, such as material compositions and widths. For example, I choose devices that produce biphotons with general desired properties, change their properties in a desired manner and detect them.

3.2. Device Modeling

In the second stage, I first model the devices physically. This is done by selecting the classical physical entities which constitute each of the devices. For example, selecting the free electron gas model for the SPDC source.

Next, I model the devices mathematically. This is done by selecting the mathematical description of each device which corresponds to its physical model, in the sense that the same physical entity can be described by different mathematical models. For example, writing the classical equations of motion of the electrons constituting the SPDC source.

Next, I represent each device by a transfer relation, which is a relation between the physical quantities of interest at the outputs and at the inputs of the device. This is done by calculating the desired relations from the mathematical model. For example, I calculate the transfer matrix relating the complex field amplitudes at the two outputs of the beam splitter to the amplitudes at its two inputs.

Finally, I represent each device by a quantum transfer relation, which is a relation between the ladder operators at the outputs and at the inputs of the devices. This is done by using the quantization procedure described earlier, which can be performed at different points during the steps for convenience. For example, I can first quantize the classical equations and then find the transfer matrix in terms of the ladder operators. Alternatively, I can take a transfer matrix that relates the complex amplitudes of the electric fields, which is obtained from the classical model, and consider it valid for the quantum case, since the ladder operators are proportional to the complex amplitudes.

3.3. Coincidence Count Rate Calculation

In the third stage, I first calculate the ladder operators at the output of the SPDC source and express them in terms of the operators at its input. This is done by using the quantum transfer relation representing the device. It allows calculating expectation values of interest in the Heisenberg picture at the output of the system, and when all of the operators inside an expectation value are at the same z , the vacuum expectation values described by Eq. (2.2.12) can be used.

Next, I calculate the second order correlation function at the output of the SPDC source in the Heisenberg picture. This is done by plugging the ladder operators at the output of the source along with the wave function at the input of the source into Eq. (2.5.1). I proceed to move between the real and frequency domains when needed by using Fourier transforms and then I simplify the expression analytically as much as possible. I do so by looking at the general term in the expectation value and finding which terms nullify, using the vacuum expectation values presented in Eq. (2.2.12), integrating the resulting expression while using the properties of the delta function and finally organizing the expression.

Next, I calculate the coincidence count rate at the output of the SPDC source. This is done by plugging the second order correlation function into Eq. (2.5.3). I proceed to simplify the expression analytically as much as possible by integrating it and using the definition of the delta function. The resulting expression for the coincidence count rate depends on the parameters of the device.

Next, I calculate the coincidence count rate at the output of the HOM system. This is done by repeating the steps taken to calculate the coincidence count rate at the output of the SPDC source.

Finally, I calculate the expression for the probability amplitude in the wave function representation of the SPDC source. This is done by comparing two expressions for the coincidence count rate of a system containing only an SPDC source. The first expression is the rate that is found when considering the SPDC source alone, and the second is the rate that is found when considering the entire HOM system while removing all of the devices except the source, by appropriate substitutions. For example, the transfer matrix representing the beam splitter is replaced by a unit matrix.

3.4. Simulations

In the last stage, I first specify an example system. This is done by selecting and calculating specific material parameters for the optical devices, which fit the design goals and reflect realistic device properties. For example, I find the width of the multilayer bilayers for the wavelength and incidence angle of the signal field at phase matching by using Eq. (2.4.5). To estimate the required number of bilayers for 100% and 50% reflectivity, thus creating an ideal mirror and beam splitter, I use Eq. (2.4.6).

Next, I calculate the coincidence count rate numerically for the example system. This is done by plugging the specific parameters into the general expression of the coincidence count rate and integrating it numerically using Mathematica.

Finally, I exhibit the HOM dip by plotting the coincidence count rate versus the delay between the biphotons.

4. Outcomes

In this section I present the outcomes of my work, showing how I have successfully designed an optical system that exhibits the x-ray HOM effect and allows the measurement of sub-attosecond delays and sub-Angstrom optical path differences. I start by presenting the schematic design I chose for the optical system, then I present the models of the optical devices comprising it, then I present how I calculated the coincidence count rate at the output of the source and the HOM system, and finally I present the simulations I performed for an example system and the HOM dip resulting from the design choices.

4.1. System Design

I now present the schematic design I have chosen for the optical system, which demonstrates the HOM effect in the x-ray regime while dealing with the different design obstacles.

When I chose the optical devices comprising the system, I had to overcome several main challenges. The source had to produce indistinguishable broadband x-ray photon pairs and have a suppressed background noise. In addition, to work in the x-ray regime, where the refractive index is approximately one and the absorption length can reach tens of nanometers, the interferometer had to be able to divert the photons and be narrower than the absorption length. Finally, the interferometer had to accommodate the wide bandwidth and angular distribution of the source, which was based on SPDC.

The proposed optical system is comprised of a biphoton source, a phase shifter, two mirrors, a beam splitter and two detectors. The biphotons source is based on SPDC and generates indistinguishable photon pairs, one of which passes through a phase shifter, which creates a delay between the biphotons. The biphotons are then redirected by multilayer mirrors into a multilayer beam splitter, and finally they are detected by two photodetectors, found at the outputs of the beam splitter. The Bragg angles of the multilayer devices match the separation angle of the biphotons, so the setup forms a parallelogram shape which allows the biphotons to arrive simultaneously to the beam splitter when the delay is zero. This can be seen in Fig. 5:

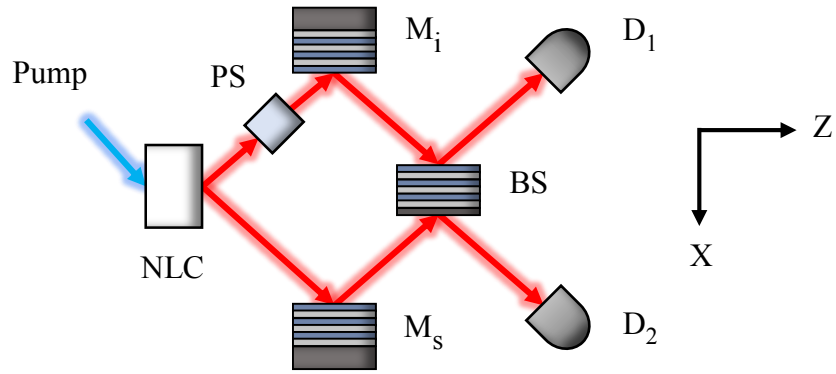


FIG. 5. Schematic diagram of the proposed experimental system. The pump photons are down-converted in a nonlinear crystal (NLC) into signal and idler photon pairs and the idler photon propagates through a phase shifter (PS). The biphotons are then reflected by their corresponding multilayer mirrors (M_i and M_s) into a beam splitter (BS) and the coincidence count rate at its output is measured by two detectors (D_1 and D_2).

4.2. Device Modeling

I now describe how the optical devices composing the HOM system were modeled physically and mathematically. The model of the SPDC source is presented first, then the phase shifter, then the multilayer beam splitter and mirrors, and finally I present the model of the photodetectors.

4.2.1. SPDC Source Model

I physically modeled the nonlinear crystal which constitutes the SPDC using the free electron gas model.

As shown earlier, the resulting mathematical model is a set of Heisenberg coupled equations for the signal and idler ladder operators in the frequency domain:

$$\begin{cases} \frac{\partial \hat{a}_s}{\partial z} = \kappa \hat{a}_i^\dagger e^{i\Delta k_z z} \\ \frac{\partial \hat{a}_i^\dagger}{\partial z} = \kappa^* \hat{a}_s e^{-i\Delta k_z z} \end{cases} \quad (4.2.1)$$

Based on this model, I calculated two mathematical models of the source, for convenience in the analytical calculations. These models are related and are expressed one in terms of the other in section 4.3.5. The first representation is the transfer matrix representation, which relates the ladder operators at the input and output ports of the source by a matrix. It was used in the calculation of the coincidence count at its output. The second representation of the source is the wave function representation, which describes the output of the source by a superposition of the vacuum state and the biphoton state. It was used in the calculation of the coincidence count of the entire HOM system.

I have denoted the general form of the transfer matrix by:

$$\begin{pmatrix} \hat{a}_s(\vec{q}_s, \omega_s) \\ \hat{a}_i^\dagger(\vec{q}_i, \omega_i) \end{pmatrix} = \begin{pmatrix} A(\vec{q}_s, \omega_s) & B(\vec{q}_s, \omega_s) \\ C(\vec{q}_s, \omega_s) & D(\vec{q}_s, \omega_s) \end{pmatrix} \begin{pmatrix} \hat{a}_{s0}(\vec{q}_s, \omega_s) \\ \hat{a}_{i0}^\dagger(\vec{q}_i, \omega_i) \end{pmatrix}, \quad (4.2.2)$$

where \hat{a}_{j0} and \hat{a}_j the frequency domain ladder operators corresponding to mode j before and after the device, respectively, and A , B , C and D are the coefficients relating the output to the input. Notice that the frequency dependencies of the operators of each of the fields are different and that the z -dependence is not written explicitly, since both of the input and output ports are at the same z .

To calculate the transfer matrix from the coupled equations, I began by assuming the conversion rate of the pump photons to signal and idler biphotons is very low, and thus the change of the operators depending on space is small. That allowed me to set $\hat{a}_{s,i} = \hat{a}_{s,i}(0)$:

$$\begin{cases} \frac{\partial \hat{a}_s}{\partial z} = \kappa \hat{a}_i^\dagger(0) e^{i\Delta k_z z} \\ \frac{\partial \hat{a}_i^\dagger}{\partial z} = \kappa^* \hat{a}_s(0) e^{-i\Delta k_z z} \end{cases}. \quad (4.2.3)$$

Integrating the coupled equations and plugging in the boundary conditions resulted in the following integration constants:

$$\begin{cases} \hat{a}_s(z) = \kappa \hat{a}_i^\dagger(0) \frac{e^{i\Delta k_z z}}{i\Delta k_z} + C_s, & C_s = \hat{a}_s(0) - \frac{\kappa \hat{a}_i^\dagger(0)}{i\Delta k_z} \\ \hat{a}_i^\dagger(z) = \kappa^* \hat{a}_s(0) \frac{e^{-i\Delta k_z z}}{-i\Delta k_z} + C_i, & C_i = \hat{a}_i^\dagger(0) + \frac{\kappa^* \hat{a}_s(0)}{i\Delta k_z} \end{cases}. \quad (4.2.4)$$

Performing some algebraic manipulations led to the following expressions:

$$\begin{cases} \hat{a}_s(z) = \hat{a}_s(0) + 2\kappa e^{\frac{i\Delta k_z z}{2}} \frac{z}{2} \operatorname{sinc}\left(\frac{\Delta k_z z}{2}\right) \hat{a}_i^\dagger(0) \\ \hat{a}_i^\dagger(z) = 2\kappa^* e^{-\frac{i\Delta k_z z}{2}} \frac{z}{2} \operatorname{sinc}\left(\frac{\Delta k_z z}{2}\right) \hat{a}_s(0) + \hat{a}_i^\dagger(0) \end{cases}, \quad (4.2.5)$$

where $\operatorname{sinc}(x) = \sin(x)/x$.

I moved into a matrix form and plugged in $z = L$ to acquire the transfer matrix:

$$\begin{pmatrix} \hat{a}_s(z) \\ \hat{a}_i^\dagger(z) \end{pmatrix} = \begin{pmatrix} 1 & \kappa z e^{\frac{i\Delta k_z z}{2}} \operatorname{sinc}\left(\frac{\Delta k_z z}{2}\right) \\ \kappa^* z e^{-\frac{i\Delta k_z z}{2}} \operatorname{sinc}\left(\frac{\Delta k_z z}{2}\right) & 1 \end{pmatrix} \begin{pmatrix} \hat{a}_s(0) \\ \hat{a}_i^\dagger(0) \end{pmatrix}, \quad (4.2.6)$$

therefore:

$$\begin{pmatrix} A & B \\ C & D \end{pmatrix} \equiv \begin{pmatrix} 1 & \kappa L e^{\frac{i\Delta k_z L}{2}} \operatorname{sinc}\left(\frac{\Delta k_z L}{2}\right) \\ \kappa^* L e^{-\frac{i\Delta k_z L}{2}} \operatorname{sinc}\left(\frac{\Delta k_z L}{2}\right) & 1 \end{pmatrix}. \quad (4.2.7)$$

This result matches the expectation of a small deviation from the initial value, which is expected since: $\kappa \ll 1$, which causes a small deviation from the initial value.

Modeling the source with an output wave function was done by the following general expression, which contains a superposition of the vacuum state and the biphoton state:

$$|\Psi\rangle_{Source} = C|0\rangle + \int d\vec{q}_s d\omega_s d\vec{q}_i d\omega_i f(\vec{q}_s, \omega_s, \vec{q}_i, \omega_i) \hat{a}_s^\dagger(\vec{q}_s, \omega_s) \hat{a}_i^\dagger(\vec{q}_i, \omega_i) |0\rangle. \quad (4.2.8)$$

Here $\hat{a}_j^\dagger(\vec{q}_j, \omega_j)$ is the creation operator of photon j in mode (\vec{q}_j, ω_j) and the z -dependence is not written explicitly again. C and $f(\vec{q}_s, \omega_s, \vec{q}_i, \omega_i)$ are the probability amplitudes to detect the vacuum state and the frequency domain biphoton state, respectively. $|C|^2$ and $|f(\vec{q}_s, \omega_s, \vec{q}_i, \omega_i)|^2$ are thus the probability to detect the vacuum state and the biphoton

probability density to detect a signal with the properties \vec{q}_s and ω_s and an idler with \vec{q}_i and ω_i , respectively. As SPDC is very inefficient, $|C|^2 \gg \int d\vec{q}_s d\omega_s d\vec{q}_i d\omega_i |f(\vec{q}_s, \omega_s, \vec{q}_i, \omega_i)|^2$.

I have denoted the biphoton wave function by:

$$|\Psi\rangle_{Biphotons} = \int d\vec{q}_s d\omega_s d\vec{q}_i d\omega_i f(\vec{q}_s, \omega_s, \vec{q}_i, \omega_i) \hat{a}_s^\dagger(\vec{q}_s, \omega_s) \hat{a}_i^\dagger(\vec{q}_i, \omega_i) |0\rangle. \quad (4.2.9)$$

As mentioned, the biphotons conserve energy:

$$\hbar\omega_p = \hbar\omega_s + \hbar\omega_i, \quad (4.2.10)$$

and conserve momentum in the x and y directions:

$$\vec{q}_p + \vec{G} = \vec{q}_s + \vec{q}_i. \quad (4.2.11)$$

These conservations were incorporated by writing:

$$f(\vec{q}_s, \omega_s, \vec{q}_i, \omega_i) = \varphi(\vec{q}_s, \omega_s) \delta(\vec{q}_i - (\vec{q}_p + \vec{G} - \vec{q}_s)) \delta(\omega_i - (\omega_p - \omega_s)). \quad (4.2.12)$$

Plugging this expression into the state and integrating over the idler variables resulted in the following final form:

$$|\Psi\rangle_{Biphotons} = \int d\vec{q} d\omega \varphi(\vec{q}, \omega) \hat{a}_s^\dagger(k_x, k_y, \omega) \hat{a}_i^\dagger(k_{px} - G_x - k_x, -k_y, \omega_p - \omega) |0\rangle. \quad (4.2.13)$$

4.2.2. Phase Shifter Model

I physically modeled the phase shifter as composed of a homogeneous isotropic linear lossless dielectric material. When such a material is placed in the path of the idler photon, the optical paths of the signal and the idler are no longer equal, and thus a delay is introduced between the biphotons.

Delaying a wave is described classically by the addition of an appropriate phase to it. Therefore, I represented the phase shifter mathematically using the following transformation, which is the common approach [32]:

$$\hat{a}_i^\dagger(k_x, k_y, \omega) \rightarrow \hat{a}_{iT}^\dagger(k_x, k_y, \omega)e^{-i\omega T}. \quad (4.2.14)$$

Here \hat{a}_i^\dagger and \hat{a}_{iT}^\dagger are the frequency domain idler creation operators before and after the device, respectively, and T is the duration of the delay between the biphotons.

4.2.3. Multilayer Optical Devices Model

I physically modeled the multilayer mirrors and the multilayer beam splitter as composed of homogeneous isotropic linear lossless dielectric layers.

For their mathematical representation, I used a transfer matrix that relates their input and output ladder operators. To find it, I first used the multilayer matrix theory [43] to calculate their classical transfer matrices, which relate the complex field amplitudes at their inputs and outputs, and then I used the aforementioned quantization procedure to obtain the quantum transfer matrix.

To find the classical transfer matrix of a device, I divided it into a stack of adjacent subsystems, such as layers and boundaries, and described every subsystem by its own transfer matrix. The multilayer devices comprise of N spacer-absorber bilayers which are deposited on a substrate. Therefore, the subsystems were as follows: The environment in which the multilayer is found, the boundary between the environment and the top-most absorber layer, the absorber layer, the boundary between the absorber and the spacer underneath it, the spacer layer, the boundary between the spacer and the absorber underneath it, the boundary between the lowest spacer and the substrate, the substrate layer, the boundary between the substrate and the environment underneath it, and finally the bottom environment.

The propagation of radiation through a homogeneous layer causes a phase shift, and was described by:

$$\begin{pmatrix} e^{inkd\cos(\theta)} & 0 \\ 0 & e^{-inkd\cos(\theta)} \end{pmatrix}, \quad (4.2.15)$$

where n is the refractive index, k is the wave number, d is the width of the layer, and θ is the propagation angle, measured from the optical axis.

The passage of the radiation through a boundary between two media was described using Fresnel's laws. For S polarization I used:

$$\frac{1}{n_1 \cos(\theta_1) + n_2 \cos(\theta_2)} \begin{pmatrix} 2n_1 \cos(\theta_1) & n_2 \cos(\theta_2) - n_1 \cos(\theta_1) \\ n_1 \cos(\theta_1) - n_2 \cos(\theta_2) & 2n_2 \cos(\theta_2) \end{pmatrix}, \quad (4.2.16)$$

where n_1 and n_2 are the refractive indices of the top and the bottom material, respectively, and θ_1 and θ_2 are the radiation propagation angles relative to the optical axis, respectively, which are related by Snell's law.

I used Mathematica to multiply the transfer matrices of all the subsystems according to the multilayer matrix theory, and the resulting transfer relation is presented here in symbolic shorthand notation. Upon calculating the total classical transfer matrix, the quantum transfer

matrix was readily given by the same expression, since in the quantization procedure the field amplitudes are proportional to the ladder operators.

The transfer relation representing the mirrors using their amplitude reflectivity was denoted as follows:

$$\begin{cases} \hat{a}_1(k_x, k_y, \omega) = M_i(-k_x, k_y, \omega)\hat{a}_{iT}(-k_x, k_y, \omega) \\ \hat{a}_2(-k_x, k_y, \omega) = M_s(k_x, k_y, \omega)\hat{a}_{sT}(k_x, k_y, \omega) \end{cases}, \quad (4.2.17)$$

where \hat{a}_2 and \hat{a}_1 are the frequency domain destruction operators at the output of the signal and idler mirror, respectively, \hat{a}_{sT} and \hat{a}_{iT} are the destruction operators of the signal and the idler at the entrance of the mirrors, respectively, M_s and M_i are the amplitude reflectivity of the signal and idler mirrors, respectively. The directions of the wavevector components express the flipping of the x component of the wavevector by the mirrors.

The beam splitter was represented via a transfer matrix relating the frequency domain destruction operators at its input and output ports, which was denoted by:

$$\begin{pmatrix} \hat{a}_3(-k_x, k_y, \omega) \\ \hat{a}_4(k_x, k_y, \omega) \end{pmatrix} = \begin{pmatrix} E(k_x, k_y, \omega) & F(-k_x, k_y, \omega) \\ G(k_x, k_y, \omega) & H(-k_x, k_y, \omega) \end{pmatrix} \begin{pmatrix} \hat{a}_1(k_x, k_y, \omega) \\ \hat{a}_2(-k_x, k_y, \omega) \end{pmatrix}. \quad (4.2.18)$$

Here \hat{a}_3 and \hat{a}_4 are the frequency domain destruction operators at the output ports of the beam splitter, \hat{a}_1 and \hat{a}_2 are the destruction operators at the input ports of the beam splitter, and E , F , G and H are the amplitude reflectivity and transmission coefficients relating the output to the input.

4.2.4. Photodetectors Model

I physically modeled the two photodetectors as having a rectangular shape, having a detection time window with an order of magnitude of 100 ns, and being able to detect x-ray photons with an ideal detection efficiency.

I modeled them mathematically by the previously mentioned coincidence count rate formula, which describes the result of their interaction with x-ray biphotons in a coincidence measurement:

$$R_C = S \int \int G^{(2)}(\vec{r}_1, t_1, \vec{r}_2, t_2) d\vec{u} dt. \quad (4.2.19)$$

4.3. Coincidence Count Rate Calculation

I now present the analytical calculations of the coincidence count rates at the output of the SPDC source and of the entire HOM system. In the calculations, the most general mathematical representations of the optical devices were used, in order to acquire a symbolic expression for the rate in terms of the parameters representing the devices.

To perform the calculation for a given system, I first found the ladder operators at its output expressed by the operators at its input, in order to work in the Heisenberg picture. Then I calculated the second order correlation function, and finally I integrated the correlation function over the parameters of a detector positioned at the output of the system, to obtain the coincidence count rate.

4.3.1. SPDC Source Coincidence Count Rate

I began with the calculation of the coincidence count rate at the output of the SPDC source. This expands upon previous similar calculations by the use of the aforementioned quantization formalism and the inclusion of the spatial dependence of the ladder operators. The result is used in section 4.3.5. to find the probability amplitude of the wave function representation of the source, which is used in turn to find the coincidence count rate of the entire HOM system.

To calculate the coincidence count rate, the second order correlation function was found first:

$$G^{(2)}(\vec{r}_1, t_1, \vec{r}_2, t_2) = \langle \Psi | \hat{a}_Y^\dagger(\vec{r}_2, t_2) \hat{a}_X^\dagger(\vec{r}_1, t_1) \hat{a}_X(\vec{r}_1, t_1) \hat{a}_Y(\vec{r}_2, t_2) | \Psi \rangle. \quad (4.3.1)$$

Plugging in the wave function at the input of the source, where the signal and idler fields are at the vacuum state, and using the Fourier transforms of the time domain ladder operators, led to:

$$\begin{aligned} G^{(2)} &= \int d\vec{q}_1 d\vec{q}_2 d\vec{q}_3 d\vec{q}_4 d\omega_1 d\omega_2 d\omega_3 d\omega_4 \\ &\times e^{i(\vec{q}_1 - \vec{q}_4) \cdot \vec{r}_2} e^{-i(\omega_1 - \omega_4)t_2} e^{i(\vec{q}_2 - \vec{q}_3) \cdot \vec{r}_1} e^{-i(\omega_2 - \omega_3)t_1} \\ &\times \langle 0 | \hat{a}_i^\dagger(\vec{q}_1, \omega_1) \hat{a}_s^\dagger(\vec{q}_2, \omega_2) \hat{a}_s(\vec{q}_3, \omega_3) \hat{a}_i(\vec{q}_4, \omega_4) | 0 \rangle. \end{aligned} \quad (4.3.2)$$

To calculate the expectation value at the entrance of the system, by having all of the operators at the same z , I plugged in the expression of the SPDC output ladder operators in terms of the input operators, which are given by the transfer matrix representation of the SPDC source:

$$\begin{aligned}
G^{(2)} &= \int d\vec{q}_1 d\omega_1 d\vec{q}_2 d\omega_2 d\vec{q}_3 d\omega_3 d\vec{q}_4 d\omega_4 \\
&\times e^{i[(\vec{q}_1 - \vec{q}_4) \cdot \vec{r}_2 - (\vec{q}_3 - \vec{q}_2) \cdot \vec{r}_1]} e^{-i[(\omega_1 - \omega_4)t_2 - (\omega_3 - \omega_2)t_1]} \\
&\times \langle 0 | \left[C(\vec{q}_p + \vec{G} - \vec{q}_1, \omega_p - \omega_1) \hat{a}_{s0}(\vec{q}_p + \vec{G} - \vec{q}_1, \omega_p - \omega_1) \right. \\
&\quad \left. + D(\vec{q}_p + \vec{G} - \vec{q}_1, \omega_p - \omega_1) \hat{a}_{i0}^\dagger(\vec{q}_1, \omega_1) \right] \\
&\times [A^*(\vec{q}_2, \omega_2) \hat{a}_{s0}^\dagger(\vec{q}_2, \omega_2) + B^*(\vec{q}_2, \omega_2) \hat{a}_{i0}(\vec{q}_p + \vec{G} - \vec{q}_2, \omega_p - \omega_2)] \\
&\times [A(\vec{q}_3, \omega_3) \hat{a}_{s0}(\vec{q}_3, \omega_3) + B(\vec{q}_3, \omega_3) \hat{a}_{i0}^\dagger(\vec{q}_p + \vec{G} - \vec{q}_3, \omega_p - \omega_3)] \\
&\times [C^*(\vec{q}_p + \vec{G} - \vec{q}_4, \omega_p - \omega_4) \hat{a}_{s0}^\dagger(\vec{q}_p + \vec{G} - \vec{q}_4, \omega_p - \omega_4) \\
&\quad \left. + D^*(\vec{q}_p + \vec{G} - \vec{q}_4, \omega_p - \omega_4) \hat{a}_{i0}(\vec{q}_4, \omega_4) \right] |0\rangle. \tag{4.3.3}
\end{aligned}$$

The next step was calculating the vacuum expectation value, by finding which of its 16 terms do not nullify. The general form of the terms without the coefficients and the frequency dependencies is:

$$\langle 0 | (\hat{a}_{s0} \text{ or } \hat{a}_{i0}^\dagger) (\hat{a}_{s0}^\dagger \text{ or } \hat{a}_{i0}) (\hat{a}_{s0} \text{ or } \hat{a}_{i0}^\dagger) (\hat{a}_{s0}^\dagger \text{ or } \hat{a}_{i0}) |0\rangle. \tag{4.3.4}$$

Only two terms remained in the expectation value, those with the form $\langle 0 | \hat{a}_{s0} \hat{a}_{i0} \hat{a}_{i0}^\dagger \hat{a}_{s0}^\dagger |0\rangle$ and $\langle 0 | \hat{a}_{s0} \hat{a}_{s0}^\dagger \hat{a}_{s0} \hat{a}_{s0}^\dagger |0\rangle$.

Plugging the expectation value back into $G^{(2)}$ with the coefficients and the frequency dependencies, and then performing the vacuum expectation values, led to:

$$\begin{aligned}
G^{(2)} &= \int d\vec{q}_1 d\omega_1 d\vec{q}_2 d\omega_2 d\vec{q}_3 d\omega_3 d\vec{q}_4 d\omega_4 \\
&\times e^{i[(\vec{q}_1 - \vec{q}_4) \cdot \vec{r}_2 - (\vec{q}_3 - \vec{q}_2) \cdot \vec{r}_1]} e^{-i[(\omega_1 - \omega_4)t_2 - (\omega_3 - \omega_2)t_1]} \\
&\times [C(\vec{q}_p + \vec{G} - \vec{q}_1, \omega_p - \omega_1) B^*(\vec{q}_2, \omega_2) \\
&\quad \times B(\vec{q}_3, \omega_3) C^*(\vec{q}_p + \vec{G} - \vec{q}_4, \omega_p - \omega_4) \\
&\times \frac{1}{(2\pi)^3} \delta_{s0, s0} \delta((\vec{q}_p + \vec{G} - \vec{q}_1) - (\vec{q}_p + \vec{G} - \vec{q}_4)) \\
&\quad \times \delta((\omega_p - \omega_1) - (\omega_p - \omega_4)) \\
&\times \frac{1}{(2\pi)^3} \delta_{i0, i0} \delta((\vec{q}_p + \vec{G} - \vec{q}_2) - (\vec{q}_p + \vec{G} - \vec{q}_3)) \\
&\quad \times \delta((\omega_p - \omega_2) - (\omega_p - \omega_3)) \\
&\quad + C(\vec{q}_p + \vec{G} - \vec{q}_1, \omega_p - \omega_1) A^*(\vec{q}_2, \omega_2) \\
&\quad \times A(\vec{q}_3, \omega_3) C^*(\vec{q}_p + \vec{G} - \vec{q}_4, \omega_p - \omega_4) \tag{4.3.5}
\end{aligned}$$

$$\begin{aligned} & \times \frac{1}{(2\pi)^3} \delta_{s_0, s_0} \delta(\vec{q}_3 - (\vec{q}_p + \vec{G} - \vec{q}_4)) \delta(\omega_3 - (\omega_p - \omega_4)) \\ & \times \frac{1}{(2\pi)^3} \delta_{s_0, s_0} \delta((\vec{q}_p + \vec{G} - \vec{q}_1) - \vec{q}_2) \delta((\omega_p - \omega_1) - \omega_2) \Big]. \end{aligned}$$

I integrated over $d\vec{q}_3 d\omega_3 d\vec{q}_4 d\omega_4$ in the first term and over $d\vec{q}_2 d\omega_2 d\vec{q}_4 d\omega_4$ in the second term, and used the properties of the delta function to finally arrive to the following expression:

$$\begin{aligned} G^{(2)} &= \frac{1}{(2\pi)^6} \int d\vec{q}_1 d\omega_1 d\vec{q}_2 d\omega_2 |B(\vec{q}_2, \omega_2)|^2 |C(\vec{q}_p + \vec{G} - \vec{q}_1, \omega_p - \omega_1)|^2 \\ &+ \frac{1}{(2\pi)^6} \int d\vec{q}_1 d\omega_1 d\vec{q}_3 d\omega_3 e^{i(\vec{q}_1 + \vec{q}_3 - \vec{q}_p - \vec{G}) \cdot (\vec{r}_2 - \vec{r}_1)} e^{-i(\omega_1 + \omega_3 - \omega_p)(t_2 - t_1)} \end{aligned} \quad (4.3.6)$$

$$\times A^*(\vec{q}_p + \vec{G} - \vec{q}_1, \omega_p - \omega_1) A(\vec{q}_3, \omega_3) C(\vec{q}_p + \vec{G} - \vec{q}_1, \omega_p - \omega_1) C^*(\vec{q}_3, \omega_3).$$

Next, I turned to calculating the coincidence count rate, given by:

$$R_C(\vec{r}_1, t_1, \vec{r}_2, t_2) = S \int \int G^{(2)}(\vec{r}_1, t_1, \vec{r}_2, t_2) d\vec{u} d\tau. \quad (4.3.7)$$

Two terms exist. The term that does not depend on \vec{u} and τ is called the classical term, and it originates from accidental detection of signal and idler photons that arrive to the detectors during the detection time window. I assumed the classical term is negligible since the detection window is short enough. The rate caused by the other term, called the quantum term, is:

$$\begin{aligned} R_{C, Quantum} &= S \frac{1}{(2\pi)^6} \int d\vec{u} d\tau d\vec{q}_1 d\omega_1 d\vec{q}_3 d\omega_3 \\ &\times e^{i(\vec{q}_1 + \vec{q}_3 - \vec{q}_p - \vec{G}) \cdot (\vec{r}_2 - \vec{r}_1)} e^{-i(\omega_1 + \omega_3 - \omega_p)(t_2 - t_1)} \\ &\times A^*(\vec{q}_p + \vec{G} - \vec{q}_1, \omega_p - \omega_1) A(\vec{q}_3, \omega_3) \\ &\times C(\vec{q}_p + \vec{G} - \vec{q}_1, \omega_p - \omega_1) C^*(\vec{q}_3, \omega_3). \end{aligned} \quad (4.3.8)$$

I assumed the integration time of the detector is much longer than the biphoton correlation time, with an order of magnitude of 100 ns versus an order of magnitude of 1 as, thus the integration limits can be considered as infinite. Integrating over $d\vec{u} d\tau$ and using the definition of the delta function led to:

$$\begin{aligned} R_{C, Quantum} &= \frac{S}{(2\pi)^6} \int d\vec{q}_1 d\omega_1 d\vec{q}_3 d\omega_3 \\ &\times (2\pi)^2 \delta(\vec{q}_1 + \vec{q}_3 - \vec{q}_p - \vec{G}) 2\pi \delta(\omega_1 + \omega_3 - \omega_p) \\ &\times A^*(\vec{q}_p + \vec{G} - \vec{q}_1, \omega_p - \omega_1) A(\vec{q}_3, \omega_3) \\ &\times C(\vec{q}_p + \vec{G} - \vec{q}_1, \omega_p - \omega_1) C^*(\vec{q}_3, \omega_3). \end{aligned} \quad (4.3.9)$$

Finally, I integrated over $d\vec{q}_3 d\omega_3$, and after changing variables from $\vec{q}_p + \vec{G} - \vec{q}_1$ to \vec{q}_1 and from $\omega_p - \omega_1$ to ω_1 and removing the subscript notation “1”, the rate was found to be:

$$R_{C,Quantum} = \frac{S}{(2\pi)^3} \int d\vec{q} d\omega |A(\vec{q}, \omega) C^*(\vec{q}, \omega)|^2. \quad (4.3.10)$$

4.3.2. HOM System Output Ladder Operators

I proceeded to calculate the coincidence count rate in the Heisenberg picture, using the wave function at the input of the system, and the operators at the output of the system, after their propagation through it. I started by expressing the output operators via the input operators, which allowed me to calculate expectation values easier later, by knowing all of the operators at the same z .

Starting at the output of the system, the destruction operators in time domain after the beam splitter are:

$$\begin{aligned}\hat{a}_3(\vec{r}, t) &= \int \hat{a}_3(\vec{q}, \omega) e^{-i(\vec{q} \cdot \vec{r} - \omega t)} d\vec{q} d\omega, \\ \hat{a}_4(\vec{r}', t') &= \int \hat{a}_4(\vec{q}', \omega') e^{-i(\vec{q}' \cdot \vec{r}' - \omega' t')} d\vec{q}' d\omega'.\end{aligned}\tag{4.3.11}$$

I moved into the frequency domain using the Fourier transform, since the transfer matrix representing the beam splitter is known in the frequency domain.

Plugging in the transfer relations of the beam splitter, as denoted by Eq. (4.2.18), gave me the output operators expressed by the operators after the mirrors:

$$\begin{aligned}\hat{a}_3(\vec{r}, t) &= \int [E(-k_x, k_y, \omega) \hat{a}_1(-k_x, k_y, \omega) \\ &\quad + F(k_x, k_y, \omega) \hat{a}_2(k_x, k_y, \omega)] e^{-i(\vec{q} \cdot \vec{r} - \omega t)} d\vec{q} d\omega, \\ \hat{a}_4(\vec{r}', t') &= \int [G(k_x', k_y', \omega') \hat{a}_1(k_x', k_y', \omega') \\ &\quad + H(-k_x', k_y', \omega') \hat{a}_2(-k_x', k_y', \omega')] e^{-i(\vec{q}' \cdot \vec{r}' - \omega' t')} d\vec{q}' d\omega'.\end{aligned}\tag{4.3.12}$$

Similarly, plugging in the input-output relations of the mirror, as denoted by Eq. (4.2.17), gave me the output operators expressed by the operators after the phase shifter:

$$\begin{aligned}\hat{a}_3(\vec{r}, t) &= \int [E(-k_x, k_y, \omega) M_i(k_x, k_y, \omega) \hat{a}_{iT}(k_x, k_y, \omega) \\ &\quad + F(k_x, k_y, \omega) M_s(-k_x, k_y, \omega) \hat{a}_{sT}(-k_x, k_y, \omega)] e^{-i(\vec{q} \cdot \vec{r} - \omega t)} d\vec{q} d\omega, \\ \hat{a}_4(\vec{r}', t') &= \int [G(k_x', k_y', \omega') M_i(-k_x', k_y', \omega') \hat{a}_{iT}(-k_x', k_y', \omega') \\ &\quad + H(-k_x', k_y', \omega') M_s(k_x', k_y', \omega') \hat{a}_{sT}(k_x', k_y', \omega')] e^{-i(\vec{q}' \cdot \vec{r}' - \omega' t')} d\vec{q}' d\omega'.\end{aligned}\tag{4.3.13}$$

Finally, plugging in the transformation of the phase shifter, given by Eq. (4.2.14), gave the output operators expressed by the operators after the SPDC source:

$$\begin{aligned}
& \hat{a}_3(\vec{r}, t) \\
&= \int [E(-k_x, k_y, \omega)M_i(k_x, k_y, \omega)\hat{a}_i(k_x, k_y, \omega)e^{-i\omega T} \\
&+ F(k_x, k_y, \omega)M_s(-k_x, k_y, \omega)\hat{a}_s(-k_x, k_y, \omega)]e^{-i(\vec{q}\cdot\vec{r}-\omega t)}d\vec{q}d\omega, \\
& \hat{a}_4(\vec{r}, t) \\
&= \int [G(k_x, k_y, \omega)M_i(-k_x, k_y, \omega)\hat{a}_i(-k_x, k_y, \omega)e^{-i\omega T} \\
&+ H(-k_x, k_y, \omega)M_s(k_x, k_y, \omega)\hat{a}_s(k_x, k_y, \omega)]e^{-i(\vec{q}\cdot\vec{r}-\omega t)}d\vec{q}d\omega.
\end{aligned} \tag{4.3.14}$$

4.3.3. HOM System Second Order Correlation Function

Having found the output operators, I calculated the second order correlation function:

$$G^{(2)}(\vec{r}_1, t_1, \vec{r}_2, t_2) = \langle \Psi | \hat{a}_Y^\dagger(\vec{r}_2, t_2) \hat{a}_X^\dagger(\vec{r}_1, t_1) \hat{a}_X(\vec{r}_1, t_1) \hat{a}_Y(\vec{r}_2, t_2) | \Psi \rangle. \quad (4.3.15)$$

I plugged in the input wave function, given by Eq. (4.2.13), and the output operators in terms of the input operators, given by Eq. (4.3.14), and denoted the different frequency variables with the subscripts 1-6, according to their order of appearance:

$$\begin{aligned} G^{(2)} &= \langle 0 | \int d\vec{q}_1 d\omega_1 \varphi^*(\vec{q}_1, \omega_1) \\ &\quad \times \hat{a}_i(k_{px} - G_x - k_{1x}, -k_{1y}, \omega_p - \omega_1) \hat{a}_s(k_{1x}, k_{1y}, \omega_1) \\ &\quad \times \int [G^*(k_{2x}, k_{2y}, \omega_2) M_i^*(-k_{2x}, k_{2y}, \omega_2) \hat{a}_i^\dagger(-k_{2x}, k_{2y}, \omega_2) e^{i\omega_2 T} \\ &\quad + H^*(-k_{2x}, k_{2y}, \omega_2) M_s^*(k_{2x}, k_{2y}, \omega_2) \hat{a}_s^\dagger(k_{2x}, k_{2y}, \omega_2)] e^{i(\vec{q}_2 \cdot \vec{r}_2 - \omega_2 t_2)} d\vec{q}_2 d\omega_2 \\ &\quad \times \int [E^*(-k_{3x}, k_{3y}, \omega_3) M_i^*(k_{3x}, k_{3y}, \omega_3) \hat{a}_i^\dagger(k_{3x}, k_{3y}, \omega_3) e^{i\omega_3 T} \\ &\quad + F^*(k_{3x}, k_{3y}, \omega_3) M_s^*(-k_{3x}, k_{3y}, \omega_3) \hat{a}_s^\dagger(-k_{3x}, k_{3y}, \omega_3)] e^{i(\vec{q}_3 \cdot \vec{r}_1 - \omega_3 t_1)} d\vec{q}_3 d\omega_3 \\ &\quad \times \int [E(-k_{4x}, k_{4y}, \omega_4) M_i(k_{4x}, k_{4y}, \omega_4) \hat{a}_i(k_{4x}, k_{4y}, \omega_4) e^{-i\omega_4 T} \\ &\quad + F(k_{4x}, k_{4y}, \omega_4) M_s(-k_{4x}, k_{4y}, \omega_4) \hat{a}_s(-k_{4x}, k_{4y}, \omega_4)] e^{-i(\vec{q}_4 \cdot \vec{r}_1 - \omega_4 t_1)} d\vec{q}_4 d\omega_4 \\ &\quad \times \int [G(k_{5x}, k_{5y}, \omega_5) M_i(-k_{5x}, k_{5y}, \omega_5) \hat{a}_i(-k_{5x}, k_{5y}, \omega_5) e^{-i\omega_5 T} \\ &\quad + H(-k_{5x}, k_{5y}, \omega_5) M_s(k_{5x}, k_{5y}, \omega_5) \hat{a}_s(k_{5x}, k_{5y}, \omega_5)] e^{-i(\vec{q}_5 \cdot \vec{r}_2 - \omega_5 t_2)} d\vec{q}_5 d\omega_5 \\ &\quad \times \int d\vec{q}_6 d\omega_6 \varphi^*(\vec{q}_6, \omega_6) \\ &\quad \times \hat{a}_s^\dagger(k_{6x}, k_{6y}, \omega_6) \hat{a}_i^\dagger(k_{px} - G_x - k_{6x}, -k_{6y}, \omega_p - \omega_6) | 0 \rangle \end{aligned} \quad (4.3.16)$$

In addition, I changed the form of the exponents to separate the space and time dependencies:

$$\begin{aligned} &e^{i(\vec{q}_2 \cdot \vec{r}_2 - \omega_2 t_2)} e^{i(\vec{q}_3 \cdot \vec{r}_1 - \omega_3 t_1)} e^{-i(\vec{q}_4 \cdot \vec{r}_1 - \omega_4 t_1)} e^{-i(\vec{q}_5 \cdot \vec{r}_2 - \omega_5 t_2)} \\ &= e^{i[(k_{2x}, k_{2y}) - (k_{5x}, k_{5y})] \cdot \vec{r}_2 - [(k_{4x}, k_{4y}) - (k_{3x}, k_{3y})] \cdot \vec{r}_1} e^{-i[(\omega_2 - \omega_5)t_2 - (\omega_4 - \omega_3)t_1]} \end{aligned} \quad (4.3.17)$$

Next, I gathered the integrals and the exponents outside of the expectation value and looked at the general term in the expectation value to find which terms nullify and which remain. The general term has the following form:

$$\langle 0 | \hat{a}_i \hat{a}_s (\hat{a}_s^\dagger \text{ or } \hat{a}_i^\dagger) (\hat{a}_s^\dagger \text{ or } \hat{a}_i^\dagger) (\hat{a}_s \text{ or } \hat{a}_i) (\hat{a}_s \text{ or } \hat{a}_i) \hat{a}_s^\dagger \hat{a}_i^\dagger | 0 \rangle, \quad (4.3.18)$$

and only 4 terms remained:

$$\begin{aligned}
& \langle 0 | \hat{a}_i \hat{a}_s (\hat{a}_s^\dagger \hat{a}_i^\dagger \hat{a}_s \hat{a}_i) \hat{a}_s^\dagger \hat{a}_i^\dagger | 0 \rangle + \langle 0 | \hat{a}_i \hat{a}_s (\hat{a}_s^\dagger \hat{a}_i^\dagger \hat{a}_i \hat{a}_s) \hat{a}_s^\dagger \hat{a}_i^\dagger | 0 \rangle \\
& + \langle 0 | \hat{a}_i \hat{a}_s (\hat{a}_i^\dagger \hat{a}_s^\dagger \hat{a}_s \hat{a}_i) \hat{a}_s^\dagger \hat{a}_i^\dagger | 0 \rangle + \langle 0 | \hat{a}_i \hat{a}_s (\hat{a}_i^\dagger \hat{a}_s^\dagger \hat{a}_i \hat{a}_s) \hat{a}_s^\dagger \hat{a}_i^\dagger | 0 \rangle.
\end{aligned} \tag{4.3.19}$$

Or explicitly, the expectation value EV is:

$$\begin{aligned}
& EV \\
& = H^*(-k_{2x}, k_{2y}, \omega_2) M_s^*(k_{2x}, k_{2y}, \omega_2) E^*(-k_{3x}, k_{3y}, \omega_3) M_i^*(k_{3x}, k_{3y}, \omega_3) e^{i\omega_3 T} \\
& \times F(k_{4x}, k_{4y}, \omega_4) M_s(-k_{4x}, k_{4y}, \omega_4) G(k_{5x}, k_{5y}, \omega_5) M_i(-k_{5x}, k_{5y}, \omega_5) e^{-i\omega_5 T} \\
& \times \langle 0 | \hat{a}_i(k_{px} - G_x - k_{1x}, -k_{1y}, \omega_p - \omega_1) \hat{a}_s(k_{1x}, k_{1y}, \omega_1) \\
& \times \hat{a}_s^\dagger(k_{2x}, k_{2y}, \omega_2) \hat{a}_i^\dagger(k_{3x}, k_{3y}, \omega_3) \hat{a}_s(-k_{4x}, k_{4y}, \omega_4) \hat{a}_i(-k_{5x}, k_{5y}, \omega_5) \\
& \times \hat{a}_s^\dagger(k_{6x}, k_{6y}, \omega_6) \hat{a}_i^\dagger(k_{px} - G_x - k_{6x}, -k_{6y}, \omega_p - \omega_6) | 0 \rangle \\
& + H^*(-k_{2x}, k_{2y}, \omega_2) M_s^*(k_{2x}, k_{2y}, \omega_2) E^*(-k_{3x}, k_{3y}, \omega_3) M_i^*(k_{3x}, k_{3y}, \omega_3) e^{i\omega_3 T} \\
& \times E(-k_{4x}, k_{4y}, \omega_4) M_i(k_{4x}, k_{4y}, \omega_4) e^{-i\omega_4 T} H(-k_{5x}, k_{5y}, \omega_5) M_s(k_{5x}, k_{5y}, \omega_5) \\
& \times \langle 0 | \hat{a}_i(k_{px} - G_x - k_{1x}, -k_{1y}, \omega_p - \omega_1) \hat{a}_s(k_{1x}, k_{1y}, \omega_1) \\
& \times \hat{a}_s^\dagger(k_{2x}, k_{2y}, \omega_2) \hat{a}_i^\dagger(k_{3x}, k_{3y}, \omega_3) \hat{a}_i(k_{4x}, k_{4y}, \omega_4) \hat{a}_s(k_{5x}, k_{5y}, \omega_5) \\
& \times \hat{a}_s^\dagger(k_{6x}, k_{6y}, \omega_6) \hat{a}_i^\dagger(k_{px} - G_x - k_{6x}, -k_{6y}, \omega_p - \omega_6) | 0 \rangle \\
& + G^*(k_{2x}, k_{2y}, \omega_2) M_i^*(-k_{2x}, k_{2y}, \omega_2) e^{i\omega_2 T} F^*(k_{3x}, k_{3y}, \omega_3) M_s^*(-k_{3x}, k_{3y}, \omega_3) \\
& \times F(k_{4x}, k_{4y}, \omega_4) M_s(-k_{4x}, k_{4y}, \omega_4) G(k_{5x}, k_{5y}, \omega_5) M_i(-k_{5x}, k_{5y}, \omega_5) e^{-i\omega_5 T} \\
& \times \langle 0 | \hat{a}_i(k_{px} - G_x - k_{1x}, -k_{1y}, \omega_p - \omega_1) \hat{a}_s(k_{1x}, k_{1y}, \omega_1) \\
& \times \hat{a}_i^\dagger(-k_{2x}, k_{2y}, \omega_2) \hat{a}_s^\dagger(-k_{3x}, k_{3y}, \omega_3) \hat{a}_s(-k_{4x}, k_{4y}, \omega_4) \hat{a}_i(-k_{5x}, k_{5y}, \omega_5) \\
& \times \hat{a}_s^\dagger(k_{6x}, k_{6y}, \omega_6) \hat{a}_i^\dagger(k_{px} - G_x - k_{6x}, -k_{6y}, \omega_p - \omega_6) | 0 \rangle \\
& + G^*(k_{2x}, k_{2y}, \omega_2) M_i^*(-k_{2x}, k_{2y}, \omega_2) e^{i\omega_2 T} F^*(k_{3x}, k_{3y}, \omega_3) M_s^*(-k_{3x}, k_{3y}, \omega_3) \\
& \times E(-k_{4x}, k_{4y}, \omega_4) M_i(k_{4x}, k_{4y}, \omega_4) e^{-i\omega_4 T} H(-k_{5x}, k_{5y}, \omega_5) M_s(k_{5x}, k_{5y}, \omega_5) \\
& \times \langle 0 | \hat{a}_i(k_{px} - G_x - k_{1x}, -k_{1y}, \omega_p - \omega_1) \hat{a}_s(k_{1x}, k_{1y}, \omega_1) \\
& \times \hat{a}_i^\dagger(-k_{2x}, k_{2y}, \omega_2) \hat{a}_s^\dagger(-k_{3x}, k_{3y}, \omega_3) \hat{a}_i(k_{4x}, k_{4y}, \omega_4) \hat{a}_s(k_{5x}, k_{5y}, \omega_5) \\
& \times \hat{a}_s^\dagger(k_{6x}, k_{6y}, \omega_6) \hat{a}_i^\dagger(k_{px} - G_x - k_{6x}, -k_{6y}, \omega_p - \omega_6) | 0 \rangle
\end{aligned} \tag{4.3.20}$$

From the vacuum expectation values, I got:

EV

$$\begin{aligned}
&= H^*(-k_{2x}, k_{2y}, \omega_2) M_s^*(k_{2x}, k_{2y}, \omega_2) E^*(-k_{3x}, k_{3y}, \omega_3) M_i^*(k_{3x}, k_{3y}, \omega_3) e^{i\omega_3 T} \\
&\times F(k_{4x}, k_{4y}, \omega_4) M_s(-k_{4x}, k_{4y}, \omega_4) G(k_{5x}, k_{5y}, \omega_5) M_i(-k_{5x}, k_{5y}, \omega_5) e^{-i\omega_5 T} \\
&\quad \times \frac{1}{(2\pi)^3} \delta_{i,i} \delta((-k_{5x}) - (k_{px} - G_x - k_{6x})) \\
&\quad \times \delta(k_{5y} - (-k_{6y})) \delta(\omega_5 - (\omega_p - \omega_6)) \\
&\times \frac{1}{(2\pi)^3} \delta_{s,s} \delta((-k_{4x}) - k_{6x}) \delta(k_{4y} - k_{6y}) \delta(\omega_4 - \omega_6) \\
&\quad \times \frac{1}{(2\pi)^3} \delta_{i,i} \delta((k_{px} - G_x - k_{1x}) - k_{3x}) \\
&\quad \times \delta((-k_{1y}) - k_{3y}) \delta((\omega_p - \omega_1) - \omega_3) \\
&\quad \times \frac{1}{(2\pi)^3} \delta_{s,s} \delta(k_{1x} - k_{2x}) \delta(k_{1y} - k_{2y}) \delta(\omega_1 - \omega_2) \\
&+ H^*(-k_{2x}, k_{2y}, \omega_2) M_s^*(k_{2x}, k_{2y}, \omega_2) E^*(-k_{3x}, k_{3y}, \omega_3) M_i^*(k_{3x}, k_{3y}, \omega_3) e^{i\omega_3 T} \\
&\times E(-k_{4x}, k_{4y}, \omega_4) M_i(k_{4x}, k_{4y}, \omega_4) e^{-i\omega_4 T} H(-k_{5x}, k_{5y}, \omega_5) M_s(k_{5x}, k_{5y}, \omega_5) \quad (4.3.21) \\
&\quad \times \frac{1}{(2\pi)^3} \delta_{i,i} \delta(k_{4x} - (k_{px} - G_x - k_{6x})) \\
&\quad \times \delta(k_{4y} - (-k_{6y})) \delta(\omega_4 - (\omega_p - \omega_6)) \\
&\times \frac{1}{(2\pi)^3} \delta_{s,s} \delta(k_{5x} - k_{6x}) \delta(k_{5y} - k_{6y}) \delta(\omega_5 - \omega_6) \\
&\quad \times \frac{1}{(2\pi)^3} \delta_{i,i} \delta((k_{px} - G_x - k_{1x}) - k_{3x}) \\
&\quad \times \delta((-k_{1y}) - k_{3y}) \delta((\omega_p - \omega_1) - \omega_3) \\
&\quad \times \frac{1}{(2\pi)^3} \delta_{s,s} \delta(k_{1x} - k_{2x}) \delta(k_{1y} - k_{2y}) \delta(\omega_1 - \omega_2) \\
&+ G^*(k_{2x}, k_{2y}, \omega_2) M_i^*(-k_{2x}, k_{2y}, \omega_2) e^{i\omega_2 T} F^*(k_{3x}, k_{3y}, \omega_3) M_s^*(-k_{3x}, k_{3y}, \omega_3) \\
&\times F(k_{4x}, k_{4y}, \omega_4) M_s(-k_{4x}, k_{4y}, \omega_4) G(k_{5x}, k_{5y}, \omega_5) M_i(-k_{5x}, k_{5y}, \omega_5) e^{-i\omega_5 T} \\
&\quad \times \frac{1}{(2\pi)^3} \delta_{i,i} \delta((-k_{5x}) - (k_{px} - G_x - k_{6x})) \\
&\quad \times \delta(k_{5y} - (-k_{6y})) \delta(\omega_5 - (\omega_p - \omega_6))
\end{aligned}$$

$$\begin{aligned}
& \times \frac{1}{(2\pi)^3} \delta_{s,s} \delta((-k_{4x}) - k_{6x}) \delta(k_{4y} - k_{6y}) \delta(\omega_4 - \omega_6) \\
& \times \frac{1}{(2\pi)^3} \delta_{s,s} \delta(k_{1x} - (-k_{3x})) \delta(k_{1y} - k_{3y}) \delta(\omega_1 - \omega_3) \\
& \quad \times \frac{1}{(2\pi)^3} \delta_{i,i} \delta\left((k_{px} - G_x - k_{1x}) - (-k_{2x})\right) \\
& \quad \times \delta\left((-k_{1y}) - k_{2y}\right) \delta\left((\omega_p - \omega_1) - \omega_2\right) \\
& + G^*(k_{2x}, k_{2y}, \omega_2) M_i^*(-k_{2x}, k_{2y}, \omega_2) e^{i\omega_2 T} F^*(k_{3x}, k_{3y}, \omega_3) M_s^*(-k_{3x}, k_{3y}, \omega_3) \\
& \times E(-k_{4x}, k_{4y}, \omega_4) M_i(k_{4x}, k_{4y}, \omega_4) e^{-i\omega_4 T} H(-k_{5x}, k_{5y}, \omega_5) M_s(k_{5x}, k_{5y}, \omega_5) \\
& \quad \times \frac{1}{(2\pi)^3} \delta_{i,i} \delta\left(k_{4x} - (k_{px} - G_x - k_{6x})\right) \\
& \quad \times \delta\left(k_{4y} - (-k_{6y})\right) \delta\left(\omega_4 - (\omega_p - \omega_6)\right) \\
& \quad \times \frac{1}{(2\pi)^3} \delta_{s,s} \delta(k_{5x} - k_{6x}) \delta(k_{5y} - k_{6y}) \delta(\omega_5 - \omega_6) \\
& \times \frac{1}{(2\pi)^3} \delta_{s,s} \delta(k_{1x} - (-k_{3x})) \delta(k_{1y} - k_{3y}) \delta(\omega_1 - \omega_3) \\
& \quad \times \frac{1}{(2\pi)^3} \delta_{i,i} \delta\left((k_{px} - G_x - k_{1x}) - (-k_{2x})\right) \\
& \quad \times \delta\left((-k_{1y}) - k_{2y}\right) \delta\left((\omega_p - \omega_1) - \omega_2\right)
\end{aligned}$$

I then plugged in the expectation value back into the expression for $G^{(2)}$, integrated over $d\vec{q}_2 d\omega_2 d\vec{q}_3 d\omega_3 d\vec{q}_4 d\omega_4 d\vec{q}_5 d\omega_5$ and used the properties of the delta function to get:

$$\begin{aligned}
G^{(2)} &= \frac{1}{(2\pi)^{12}} \int d\vec{q}_1 d\omega_1 d\vec{q}_6 d\omega_6 \varphi^*(\vec{q}_1, \omega_1) \varphi(\vec{q}_6, \omega_6) \\
&\times \left[e^{i\left[\left((k_{1x}, k_{1y}) - (-(k_{px} - G_x - k_{6x}), -k_{6y})\right) \cdot \vec{r}_2 - \left((-k_{6x}, k_{6y}) - (k_{px} - G_x - k_{1x}, -k_{1y})\right) \cdot \vec{r}_1\right]} \right. \\
&\quad \times e^{-i\left[(\omega_1 - (\omega_p - \omega_6))t_2 - (\omega_6 - (\omega_p - \omega_1))t_1\right]} \\
&\quad \times H^*(-k_{1x}, k_{1y}, \omega_1) M_S^*(k_{1x}, k_{1y}, \omega_1) \\
&\quad \times E^*(-(k_{px} - G_x - k_{1x}), -k_{1y}, \omega_p - \omega_1) \\
&\quad \times M_i^*(k_{px} - G_x - k_{1x}, -k_{1y}, \omega_p - \omega_1) e^{i(\omega_p - \omega_1)T} \\
&\quad \quad \times F(-k_{6x}, k_{6y}, \omega_6) M_S(k_{6x}, k_{6y}, \omega_6) \\
&\quad \quad \times G(-(k_{px} - G_x - k_{6x}), -k_{6y}, \omega_p - \omega_6) \\
&\quad \times M_i(k_{px} - G_x - k_{6x}, -k_{6y}, \omega_p - \omega_6) e^{-i(\omega_p - \omega_6)T} \\
&+ e^{i\left[\left((k_{1x}, k_{1y}) - (k_{6x}, k_{6y})\right) \cdot \vec{r}_2 - \left((k_{px} - G_x - k_{6x}, -k_{6y}) - (k_{px} - G_x - k_{1x}, -k_{1y})\right) \cdot \vec{r}_1\right]} \\
&\quad \times e^{-i\left[(\omega_1 - \omega_6)t_2 - ((\omega_p - \omega_6) - (\omega_p - \omega_1))t_1\right]} \\
&\quad \times H^*(-k_{1x}, k_{1y}, \omega_1) M_S^*(k_{1x}, k_{1y}, \omega_1) \\
&\quad \times E^*(-(k_{px} - G_x - k_{1x}), -k_{1y}, \omega_p - \omega_1) \\
&\quad \times M_i^*(k_{px} - G_x - k_{1x}, -k_{1y}, \omega_p - \omega_1) e^{i(\omega_p - \omega_1)T} \\
&\quad \quad \times E(-(k_{px} - G_x - k_{6x}), -k_{6y}, \omega_p - \omega_6) \\
&\quad \times M_i(k_{px} - G_x - k_{6x}, -k_{6y}, \omega_p - \omega_6) e^{-i(\omega_p - \omega_6)T} \\
&\quad \quad \times H(-k_{6x}, k_{6y}, \omega_6) M_S(k_{6x}, k_{6y}, \omega_6) \\
&+ e^{i\left[\left((-k_{px} - G_x - k_{1x}), -k_{1y}\right) - \left(-(k_{px} - G_x - k_{6x}), -k_{6y}\right) \cdot \vec{r}_2 - \left((-k_{6x}, k_{6y}) - (-k_{1x}, k_{1y})\right) \cdot \vec{r}_1\right]} \\
&\quad \times e^{-i\left[(\omega_p - \omega_1) - (\omega_p - \omega_6)t_2 - (\omega_6 - \omega_1)t_1\right]} \\
&\quad \times G^*(-(k_{px} - G_x - k_{1x}), -k_{1y}, \omega_p - \omega_1) \\
&\quad \times M_i^*(k_{px} - G_x - k_{1x}, -k_{1y}, \omega_p - \omega_1) e^{i(\omega_p - \omega_1)T} \\
&\quad \quad \times F^*(-k_{1x}, k_{1y}, \omega_1) M_S^*(k_{1x}, k_{1y}, \omega_1) \\
&\quad \quad \times F(-k_{6x}, k_{6y}, \omega_6) M_S(k_{6x}, k_{6y}, \omega_6) \\
&\quad \times G(-(k_{px} - G_x - k_{6x}), -k_{6y}, \omega_p - \omega_6)
\end{aligned} \tag{4.3.22}$$

$$\begin{aligned}
& \times M_i(k_{px} - G_x - k_{6x}, -k_{6y}, \omega_p - \omega_6) e^{-i(\omega_p - \omega_6)T} \\
& + e^{i\left[\left(-k_{px} - G_x - k_{1x}, -k_{1y}\right) \cdot \vec{r}_2 - \left(k_{px} - G_x - k_{6x}, -k_{6y}\right) \cdot \vec{r}_1\right]} \\
& \quad \times e^{-i\left[\left(\omega_p - \omega_1\right) - \omega_6\right]t_2 - \left[\left(\omega_p - \omega_6\right) - \omega_1\right]t_1} \\
& \quad \times G^*\left(-k_{px} - G_x - k_{1x}, -k_{1y}, \omega_p - \omega_1\right) \\
& \quad \times M_i^*\left(k_{px} - G_x - k_{1x}, -k_{1y}, \omega_p - \omega_1\right) e^{i(\omega_p - \omega_1)T} \\
& \quad \quad \times F^*\left(-k_{1x}, k_{1y}, \omega_1\right) M_s^*\left(k_{1x}, k_{1y}, \omega_1\right) \\
& \quad \quad \times E\left(-k_{px} - G_x - k_{6x}, -k_{6y}, \omega_p - \omega_6\right) \\
& \quad \times M_i\left(k_{px} - G_x - k_{6x}, -k_{6y}, \omega_p - \omega_6\right) e^{-i(\omega_p - \omega_6)T} \\
& \quad \quad \times H\left(-k_{6x}, k_{6y}, \omega_6\right) M_s\left(k_{6x}, k_{6y}, \omega_6\right)
\end{aligned}$$

Note that in the chosen reference frame, of the optical axis, we have: $k_{sx} = k_{ix}$, so $k_{px} = G_x$, and $k_{py} - G_y = 0$. I used this fact and organized the expression to finally obtain:

$$\begin{aligned}
G^{(2)} &= \frac{1}{(2\pi)^{12}} \int d\vec{q}_1 d\omega_1 d\vec{q}_6 d\omega_6 \varphi^*(\vec{q}_1, \omega_1) \varphi(\vec{q}_6, \omega_6) \\
&\times \left[e^{i((k_{1x}, k_{1y}) - (k_{6x}, -k_{6y})) \cdot (\vec{r}_2 - \vec{r}_1)} e^{-i(\omega_6 - (\omega_p - \omega_1))(t_2 - t_1)} e^{i(\omega_6 - \omega_1)T} \right. \\
&\quad \times M_s^*(k_{1x}, k_{1y}, \omega_1) M_s(k_{6x}, k_{6y}, \omega_6) \\
&\quad \times M_i^*(-k_{1x}, -k_{1y}, \omega_p - \omega_1) M_i(-k_{6x}, -k_{6y}, \omega_p - \omega_6) \\
&\quad \times E^*(k_{1x}, -k_{1y}, \omega_p - \omega_1) F(-k_{6x}, k_{6y}, \omega_6) \\
&\quad \times G(k_{6x}, -k_{6y}, \omega_p - \omega_6) H^*(-k_{1x}, k_{1y}, \omega_1) \\
&+ e^{i((k_{1x}, k_{1y}) - (k_{6x}, k_{6y})) \cdot (\vec{r}_2 - \vec{r}_1)} e^{-i(\omega_1 - \omega_6)(t_2 - t_1)} e^{i(\omega_6 - \omega_1)T} \\
&\quad \times M_s^*(k_{1x}, k_{1y}, \omega_1) M_s(k_{6x}, k_{6y}, \omega_6) \\
&\quad \times M_i^*(-k_{1x}, -k_{1y}, \omega_p - \omega_1) M_i(-k_{6x}, -k_{6y}, \omega_p - \omega_6) \\
&\quad \times E^*(k_{1x}, -k_{1y}, \omega_p - \omega_1) E(k_{6x}, -k_{6y}, \omega_p - \omega_6) \\
&\quad \times H^*(-k_{1x}, k_{1y}, \omega_1) H(-k_{6x}, k_{6y}, \omega_6) \tag{4.3.23} \\
&+ e^{i((k_{1x}, -k_{1y}) - (k_{6x}, -k_{6y})) \cdot (\vec{r}_2 - \vec{r}_1)} e^{-i(\omega_6 - \omega_1)(t_2 - t_1)} e^{i(\omega_6 - \omega_1)T} \\
&\quad \times M_s^*(k_{1x}, k_{1y}, \omega_1) M_s(k_{6x}, k_{6y}, \omega_6) \\
&\quad \times M_i^*(-k_{1x}, -k_{1y}, \omega_p - \omega_1) M_i(-k_{6x}, -k_{6y}, \omega_p - \omega_6) \\
&\quad \times F^*(-k_{1x}, k_{1y}, \omega_1) F(-k_{6x}, k_{6y}, \omega_6) \\
&\quad \times G^*(k_{1x}, -k_{1y}, \omega_p - \omega_1) G(k_{6x}, -k_{6y}, \omega_p - \omega_6) \\
&+ e^{i((k_{1x}, -k_{1y}) - (k_{6x}, k_{6y})) \cdot (\vec{r}_2 - \vec{r}_1)} e^{-i((\omega_p - \omega_1) - \omega_6)(t_2 - t_1)} e^{i(\omega_6 - \omega_1)T} \\
&\quad \times M_s^*(k_{1x}, k_{1y}, \omega_1) M_s(k_{6x}, k_{6y}, \omega_6) \\
&\quad \times M_i^*(-k_{1x}, -k_{1y}, \omega_p - \omega_1) M_i(-k_{6x}, -k_{6y}, \omega_p - \omega_6) \\
&\quad \times E(k_{6x}, -k_{6y}, \omega_p - \omega_6) F^*(-k_{1x}, k_{1y}, \omega_1) \\
&\quad \times G^*(k_{1x}, -k_{1y}, \omega_p - \omega_1) H(-k_{6x}, k_{6y}, \omega_6) \left. \right]
\end{aligned}$$

4.3.4. HOM System Coincidence Count Rate

Having acquired the second order correlation function, I plugged it into the coincidence count rate formula:

$$R_C = S \int \int G^{(2)}(\vec{r}_1, t_1, \vec{r}_2, t_2) d\vec{u} d\tau \quad (4.3.24)$$

Since the integration time of the detector is much longer than the correlation time of the biphotons, where the orders of magnitude of these time intervals are 100 ns versus 1 as, I could assume the boundaries of the integral are infinite.

I integrated over $d\vec{u} d\tau$ and used the definition of the delta function, to get:

$$\begin{aligned} R_C = S \frac{1}{(2\pi)^{12}} \int d\vec{q}_1 d\omega_1 d\vec{q}_6 d\omega_6 \varphi^*(\vec{q}_1, \omega_1) \varphi(\vec{q}_6, \omega_6) \\ \times \left[2\pi\delta(k_{1x} - k_{6x}) 2\pi\delta(k_{1y} - (-k_{6y})) 2\pi\delta(\omega_6 - (\omega_p - \omega_1)) e^{i(\omega_6 - \omega_1)T} \right. \\ \quad \times M_s^*(k_{1x}, k_{1y}, \omega_1) M_s(k_{6x}, k_{6y}, \omega_6) \\ \quad \times M_i^*(-k_{1x}, -k_{1y}, \omega_p - \omega_1) M_i(-k_{6x}, -k_{6y}, \omega_p - \omega_6) \\ \quad \times E^*(k_{1x}, -k_{1y}, \omega_p - \omega_1) F(-k_{6x}, k_{6y}, \omega_6) \\ \quad \times G(k_{6x}, -k_{6y}, \omega_p - \omega_6) H^*(-k_{1x}, k_{1y}, \omega_1) \\ + 2\pi\delta(k_{1x} - k_{6x}) 2\pi\delta(k_{1y} - k_{6y}) 2\pi\delta(\omega_1 - \omega_6) e^{i(\omega_6 - \omega_1)T} \\ \quad \times M_s^*(k_{1x}, k_{1y}, \omega_1) M_s(k_{6x}, k_{6y}, \omega_6) \\ \quad \times M_i^*(-k_{1x}, -k_{1y}, \omega_p - \omega_1) M_i(-k_{6x}, -k_{6y}, \omega_p - \omega_6) \\ \quad \times E^*(k_{1x}, -k_{1y}, \omega_p - \omega_1) E(k_{6x}, -k_{6y}, \omega_p - \omega_6) \\ \quad \times H^*(-k_{1x}, k_{1y}, \omega_1) H(-k_{6x}, k_{6y}, \omega_6) \\ + 2\pi\delta(k_{1x} - k_{6x}) 2\pi\delta((-k_{1y}) - (-k_{6y})) 2\pi\delta(\omega_6 - \omega_1) e^{i(\omega_6 - \omega_1)T} \\ \quad \times M_s^*(k_{1x}, k_{1y}, \omega_1) M_s(k_{6x}, k_{6y}, \omega_6) \\ \quad \times M_i^*(-k_{1x}, -k_{1y}, \omega_p - \omega_1) M_i(-k_{6x}, -k_{6y}, \omega_p - \omega_6) \\ \quad \times F^*(-k_{1x}, k_{1y}, \omega_1) F(-k_{6x}, k_{6y}, \omega_6) \\ \quad \times G^*(k_{1x}, -k_{1y}, \omega_p - \omega_1) G(k_{6x}, -k_{6y}, \omega_p - \omega_6) \\ + 2\pi\delta(k_{1x} - k_{6x}) 2\pi\delta((-k_{1y}) - k_{6y}) 2\pi\delta((\omega_p - \omega_1) - \omega_6) e^{i(\omega_6 - \omega_1)T} \\ \quad \times M_s^*(k_{1x}, k_{1y}, \omega_1) M_s(k_{6x}, k_{6y}, \omega_6) \end{aligned} \quad (4.3.25)$$

$$\begin{aligned}
& \times M_i^*(-k_{1x}, -k_{1y}, \omega_p - \omega_1) M_i(-k_{6x}, -k_{6y}, \omega_p - \omega_6) \\
& \quad \times E(k_{6x}, -k_{6y}, \omega_p - \omega_6) F^*(-k_{1x}, k_{1y}, \omega_1) \\
& \quad \times G^*(k_{1x}, -k_{1y}, \omega_p - \omega_1) H(-k_{6x}, k_{6y}, \omega_6)
\end{aligned}$$

Next, I integrated over $d\vec{q}_6 d\omega_6$, used the properties of the delta function, organized the result and removed the subscript notation “1” to finally find the analytical expression for the coincidence count rate:

$$\begin{aligned}
R_C &= \frac{S}{(2\pi)^9} \int d\vec{q} d\omega \\
& \times \left\{ |\varphi(k_x, k_y, \omega) M_s(k_x, k_y, \omega) M_i(-k_x, -k_y, \omega_p - \omega)|^2 \right. \\
& \quad \times \left[|E(k_x, -k_y, \omega_p - \omega) H(-k_x, k_y, \omega)|^2 \right. \\
& \quad \left. \left. + |F(-k_x, k_y, \omega) G(k_x, -k_y, \omega_p - \omega)|^2 \right] \right. \\
& \quad \left. + \varphi^*(k_x, k_y, \omega) \varphi(k_x, -k_y, \omega_p - \omega) e^{i(\omega_p - 2\omega)T} \right. \\
& \quad \times M_s(k_x, -k_y, \omega_p - \omega) M_s^*(k_x, k_y, \omega) \\
& \quad \times M_i(-k_x, k_y, \omega) M_i^*(-k_x, -k_y, \omega_p - \omega) \\
& \quad \times [E(k_x, k_y, \omega) F^*(-k_x, k_y, \omega) \\
& \quad \times G^*(k_x, -k_y, \omega_p - \omega) H(-k_x, -k_y, \omega_p - \omega) \\
& \quad \left. + E^*(k_x, -k_y, \omega_p - \omega) F(-k_x, -k_y, \omega_p - \omega) \right. \\
& \quad \left. \times G(k_x, k_y, \omega) H^*(-k_x, k_y, \omega)] \right\} \tag{4.3.26}
\end{aligned}$$

4.3.5. SPDC Source Probability Amplitude

In the final step, I found the expression of the probability amplitude in the wave function representation of the SPDC source in terms of the matrix elements of the transfer matrix representation. This was done by comparing two different expressions for the coincidence count rate of a system containing only an SPDC source.

The first expression was calculated when I considered the SPDC source alone, and appears in Eq. (4.3.10):

$$R_{C,source} = \frac{S}{(2\pi)^3} \int d\vec{q}d\omega |A(\vec{q}, \omega)C^*(\vec{q}, \omega)|^2. \quad (4.3.27)$$

I calculated the second expression from the coincidence count rate of the entire HOM system by removing all of the other devices, which I did by plugging in the following transfer relations:

$$M_s = M_i = 1, \quad \begin{pmatrix} E & F \\ G & H \end{pmatrix} = \begin{pmatrix} 1 & 0 \\ 0 & 1 \end{pmatrix}. \quad (4.3.28)$$

This left me with:

$$R_{C,HOM \text{ with source only}} = \frac{S}{(2\pi)^9} \int d\vec{q}d\omega |\varphi(\vec{q}, \omega)|^2. \quad (4.3.29)$$

By comparing the expressions, the probability amplitude was found to be:

$$\varphi(\vec{q}, \omega) = (2\pi)^3 A(\vec{q}, \omega)C^*(\vec{q}, \omega). \quad (4.3.30)$$

Plugging the matrix elements of the transfer matrix representing the source into the biphoton amplitude, according to Eq. (4.2.7), gives the probability amplitude for the specific chosen model:

$$\varphi(\vec{q}, \omega) = (2\pi)^3 \kappa L e^{\frac{i\Delta k_z L}{2}} \text{sinc}\left(\frac{\Delta k_z L}{2}\right). \quad (4.3.31)$$

From the resulting expression, we see it is most probable to find the biphotons when the phase mismatch nullifies, which implies perfect phase matching. In addition, we see the proportionality to the length of the crystal and to the coupling coefficient, and the sinc-like behavior, which are all expected from nonlinear optics.

The coincidence count rate of the HOM system can now be expressed in terms of the symbolic representations of all of the optical devices:

$$\begin{aligned}
R_C = & \frac{S}{(2\pi)^3} \int d\vec{q} d\omega \\
& \times \{ |A(k_x, k_y, \omega) C^*(k_x, k_y, \omega) \\
& \times M_s(k_x, k_y, \omega) M_i(-k_x, -k_y, \omega_p - \omega)|^2 \\
& \times [|E(k_x, -k_y, \omega_p - \omega) H(-k_x, k_y, \omega)|^2 \\
& + |F(-k_x, k_y, \omega) G(k_x, -k_y, \omega_p - \omega)|^2] \\
& + A^*(k_x, k_y, \omega) C(k_x, k_y, \omega) \\
& \times A(k_x, -k_y, \omega_p - \omega) C^*(k_x, -k_y, \omega_p - \omega) e^{i(\omega_p - 2\omega)T} \\
& \times M_s(k_x, -k_y, \omega_p - \omega) M_s^*(k_x, k_y, \omega) \\
& \times M_i(-k_x, k_y, \omega) M_i^*(-k_x, -k_y, \omega_p - \omega) \\
& \times [E(k_x, k_y, \omega) F^*(-k_x, k_y, \omega) \\
& \times G^*(k_x, -k_y, \omega_p - \omega) H(-k_x, -k_y, \omega_p - \omega) \\
& + E^*(k_x, -k_y, \omega_p - \omega) F(-k_x, -k_y, \omega_p - \omega) \\
& \times G(k_x, k_y, \omega) H^*(-k_x, k_y, \omega)] \}
\end{aligned} \tag{4.3.32}$$

4.4. Simulations

I now present the simulations of the optical system that I have performed. The simulations were done using Mathematica for a chosen example system, with device parameters which fit the design goals and reflect realistic properties. The simulation of the SPDC source are presented first, then the simulation of the multilayer devices, and finally the simulation of the entire HOM system, culminating in the successful demonstration of the HOM effect.

4.4.1. SPDC Source Simulation

To demonstrate the feasibility to generate indistinguishable broadband x-ray biphotons, I considered an example of a source based on parameters that have been used in previous experiments on x-ray SPDC [33]. A diamond crystal was chosen for the nonlinear source crystal, due to its extensive use in SPDC measurements at x-ray wavelengths [22,33], narrow rocking curve, and simplicity of the theoretical model. The thickness of the crystal was 0.8 mm, and phase matching was obtained using the C(660) lattice planes.

The pump photons were polarized inside the scattering plane, their energy was 21 keV, their rate was 10^{13} photons/s, the area of the beam on the crystal was 0.4 mm^2 , and their incidence angle was slightly larger than the Bragg angle, $\theta_B = 44.609 \text{ deg}$, chosen as $\theta_B + 8 \text{ mdeg}$. This deviation was required to solve the phase matching equation for the slightly lower than one refractive indices. The coupling coefficient in this case was estimated to have an order of magnitude of 10^{-19} m^{-1} [22]. In addition, transmission (Laue) geometry was used.

I chose the central photon energy of the signal and idler photons at 10.5 keV and the solution of the phase matching equation resulted in angles of propagation of 0.976 deg and -0.976 deg with respect to the optical axis described in Fig. 5. The polarizations of the signal and idler photons were parallel, which is a result of this setup [33] and is required for indistinguishability.

I calculated the spectrum of the coincidence count rate at the output of the nonlinear crystal by integrating Eq. (4.3.10) numerically over the momentum variables, and the result is shown in Fig. 6. I chose the aperture size of the detector to be 0.4 deg , which defines the angular width of the SPDC and determines the photon energy range accepted by the detector to be $8.54 \text{ keV} - 12.89 \text{ keV}$, due to the one-to-one correspondence between the energy and the propagation direction. The resulting total rate is about 0.15 pairs/s and the bandwidth is 4.35 keV . This result agrees with the experimental results [33] and indicates on the possibility to measure delays with precision of sub-attosecond time scales.

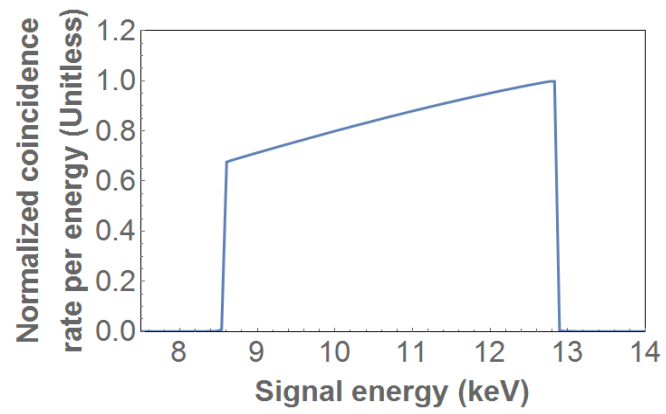


FIG. 6. The spectral dependence of the normalized coincidence count rate between the two output ports of the nonlinear crystal. The total bandwidth, which is obtained for a detector acceptance angle of 0.4 deg, is 4.35 keV.

4.4.2. Multilayer Optical Devices Simulation

Next, I present the example parameters I have chosen for the multilayer mirrors and beam splitter and their simulations. It is shown that it is possible to design optical devices with sufficient reflectivity that can accommodate the very broad angular distribution and spectrum of the generated biphotons.

I chose the absorber layers to be platinum and the spacer layers to be carbon, which are two commonly used materials [39] with a significant difference between their atomic numbers, and I assumed that the substrates are a silicon wafer. I used the data from [45] for the refractive indices and absorption coefficients. By using Eqs. (2.4.5) and (2.4.6), I found that 20 bilayers with a width of 3.7 nm and with $\Gamma = 0.5$ are sufficient to achieve an intensity reflectivity of 90% and that 10 bilayers are required to achieve approximately 50% reflectivity. For the beam splitter, the substrate width was 15 μm , which is shorter by an order of magnitude than the absorption length at 10.5 keV.

I simulated the dependence of the intensity reflectivity of the mirrors and the beam splitter on the incidence angle for 10.5 keV in Figs. 7(a) and 7(b). As expected, the simulation shows peaks in the reflectivity that obey Bragg's law. The high reflectivity at the lower angles is due to total reflection. I chose the first peak of the reflectivity at an incident angle of 0.976 deg, which is the incidence angle of the biphotons on the mirrors at perfect phase matching at the degenerate photon energy. The maximum of the reflectivity is 90% and the FWHM of the reflectivity of the mirror and the beam splitter are 0.07 deg and 0.095 deg, respectively.

Figs. 7(c) and 7(d) show the photon energy dependence of the reflectivity for an incident angle of 0.976 deg. The FWHM of the reflectivity of the mirror is 0.758 keV and of the beam splitter is 1.04 keV, whereas the bandwidth of the x-ray SPDC biphotons is 4.35 keV. Since the angular acceptance and the bandwidth of the multilayer devices are comparable to those of the biphotons, the parameters I selected enable the observation of the HOM dip at a reasonable count rate.

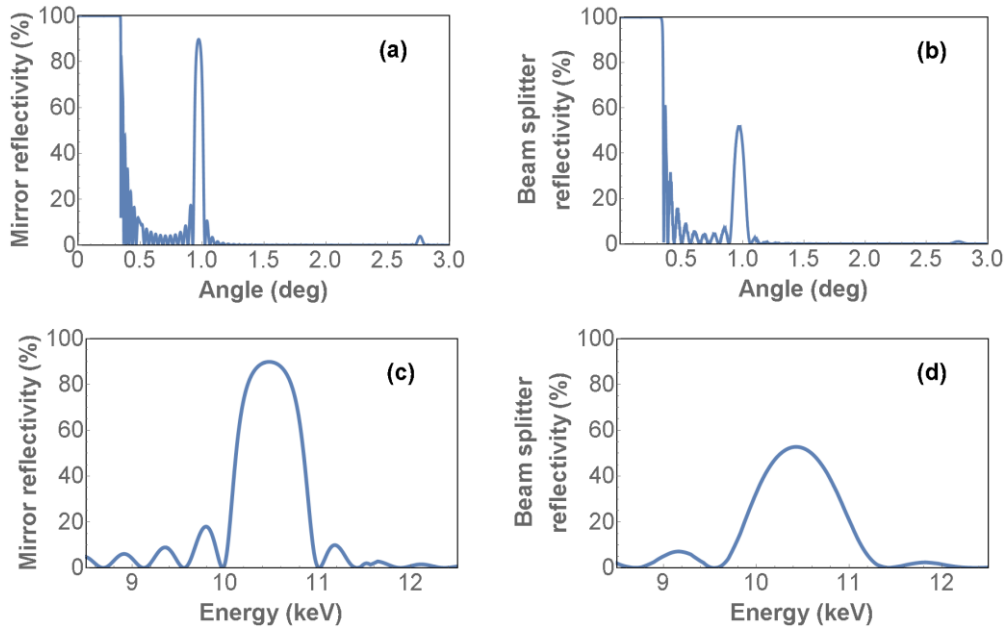


FIG. 7. The reflectivity of the multilayer mirror and the beam splitter as a function of the incidence angle, (a) and (b), and the photon energy, (c) and (d). Panels (a) and (c) show the mirror reflectivity and panels (b) and (d) the reflectivity of the beam splitter. The width of a bilayer is 3.7 nm, with $\Gamma = 0.5$.

4.4.3. HOM Interferometer Simulation

Now I turn to the main result of this work and show that the dip of x-ray HOM can be as short as 0.6 attoseconds at FWHM. To reflect realistic detector properties, I chose an aperture size of the detector of 0.4 deg. This defines the angular width of the SPDC and determines the photon energy range accepted by the detector to be 8.54 keV – 12.89 keV, due to the one-to-one correspondence between the energy and the propagation direction. I numerically calculated the integral described by Eq. (4.3.32) for various delays between the signal and the idler photons. My results are shown in Fig. 8 and are normalized to the output of the SPDC source.

It is clear that the dip of the coincidence count rate is nearly zero. The FWHM of the dip indicates on a correlation time of about 0.6 attoseconds, which corresponds to a spectral bandwidth of 1.097 keV. This ultrashort time scale corresponds to an optical path difference between the two arms of the HOM setup of about 1.8 Angstroms.

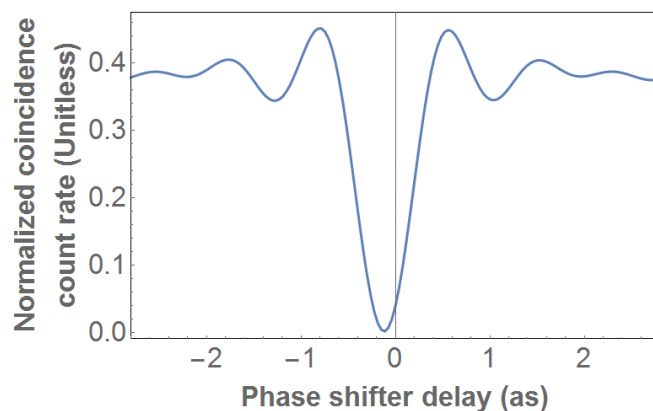


FIG. 8. The normalized coincidence count rate between the two output ports of the beam splitter as a function of the delay between the biphotons. The width of the predicted dip is about 0.6 attoseconds at FWHM. The shift from zero is due to the slight difference in the paths of the biphotons. See text for details.

5. Discussion and Summary

Reviewing the achievements of my design choices, it is evident that the design of the source ensures the generation of indistinguishable broadband x-ray biphotons with suppressed background noise, and the biphotons are indeed indistinguishable by their time of arrival to the interferometer. In addition, the design of the multilayer interferometer accommodates the broad bandwidth and angular distribution of the biphotons. Regarding the schematic design of the entire system, it has a considerable advantage over systems which demonstrate a coincidence count rate dip but include more devices – it is much easier to implement experimentally.

I note that since the mirrors are designed to have more layers than the beam splitter, the biphoton bandwidth and angular spread are limited by the mirrors. Therefore, they are narrower than the acceptance angle and the spectral bandwidth of the beam splitter (the range where the reflectivity and the transmission are almost constant). This design helps ensuring that the signal and idler photons are indistinguishable by their frequency distribution at the input of the beam splitter.

The analytical result of the coincidence count rate behaves as expected. For zero delay, the biphotons are indistinguishable by their time of arrival to the beam splitter, and the rate is expected to nullify if the biphotons are also indistinguishable by their frequency distribution. For infinite delay, the biphotons are completely distinguishable by their time of arrival to the beam splitter, and the rate is expected to be equal to half the source rate. This behavior can be demonstrated via simulations, and can be readily seen for ideal optical devices, by plugging the following representations into the result:

$$M_s = M_i = 1, \quad \begin{pmatrix} E & F \\ G & H \end{pmatrix} = \frac{1}{\sqrt{2}} \begin{pmatrix} -i & 1 \\ 1 & -i \end{pmatrix}. \quad (5.1)$$

This gives:

$$R_{C,ideal\ devices} = \frac{1}{2} \frac{S}{(2\pi)^9} \int d\vec{q} d\omega \times \left[|\varphi(k_x, k_y, \omega)|^2 - \varphi^*(k_x, k_y, \omega) \varphi(k_x, -k_y, \omega_p - \omega) e^{i(\omega_p - 2\omega)T} \right]. \quad (5.2)$$

Plugging in $T = 0$ gives:

$$R_{C,ideal\ devices} \xrightarrow{T=0} \frac{1}{2} \frac{S}{(2\pi)^9} \int d\vec{q} d\omega \times \left[|\varphi(k_x, k_y, \omega)|^2 - \varphi^*(k_x, k_y, \omega) \varphi(k_x, -k_y, \omega_p - \omega) \right]. \quad (5.3)$$

This expression nullifies if the probability amplitude is symmetrical in the following manner:

$$\varphi(k_x, -k_y, \omega_p - \omega) = \varphi(k_x, k_y, \omega), \quad (5.4)$$

which is expected since when the probability amplitude is symmetrical, then the biphotons are indistinguishable by their frequency distribution. For $T \rightarrow \infty$, the integration over a symmetrical range of the rapidly changing exponent nullifies, which gives:

$$R_{C, Ideal\ devices} \xrightarrow{T \rightarrow \infty} \frac{1}{2} \frac{S}{(2\pi)^9} \int d\vec{q} d\omega |\varphi(k_x, k_y, \omega)|^2. \quad (5.5)$$

This expression is equal to exactly half the rate of the source, as expected.

As for the simulated coincidence count rate for the proposed parameters, it also behaves as expected for the extreme values of delays between the biphotons, even though the HOM dip appears slightly different than in the ideal case. This happens exactly due to the proposed system not being ideal. Due to the losses of the SPDC biphotons in the interferometer, after normalizing the coincidence count rate by the total rate of the source, it does not reach $\frac{1}{2}$. It is important to note that when the biphotons impinge on the beam splitter, one of them propagates through the substrate first. This asymmetry leads to small differences between the amplitude reflectivity of the two beam splitter ports. This in turn is expressed as a shift in the coincidence count rate dip. It does not, however, destroy their indistinguishability, due to the intensity coefficients remaining the same for both beam splitter sides. Additionally, the probability to measure the coincident state at the beam splitter output is proportional to the difference between the intensity coefficients [1]. Since the intensity coefficients differ slightly, the dip does not reach zero completely.

I note that the energy bandwidth calculated from the simulation of the example system is wider than the bandwidth in Figs. 7(c) and 7(d). However, this is not surprising since those figures show the bandwidth for a specific incident angle, while the angular distribution of the biphotons is broad. This observation indicates on the possibility to observe even shorter dips by designing multilayer devices with an angular dispersion that matches that of the biphotons.

I emphasize that I have described by the proposed system an example of possible parameters. However, my simulations show that the x-ray HOM effect can be measured for a large range of parameters. It is clear that the design based on multilayer optics enables this broad range of options. One concern to consider is the stability of the measurements against mechanical vibrations. I stress that the stability can be improved by using narrower band optical devices or narrower detector apertures, but for the cost of widening the dip in the coincidence count rate and therefore reducing the resolution. This may be overcome by using more sophisticated data analysis procedures [19,20]. Alternatively, fabrication of the system as a monolithic structure would improve the stability significantly.

I also emphasize that while short time delays and optical path differences can be measured with x-ray interferometers [46–48], the HOM system exhibits several important advantages. Since in the HOM effect the interference is between the wave functions of the biphotons and not between classical coherent beams, the experiment can be performed by using incoherent sources, whereas standard interferometers require sources with high spatial coherence. Another advantage is the requirements for stability of the effect, which are less stringent than the requirements for interferometers. While interferometers have to be more stable than the wavelength for the entire measurement, thus on the angstrom scale for x-rays, in the HOM effect the system has to only be stable enough to maintain the biphotons indistinguishable during a detection cycle.

In summary, I have described how to implement the Hong-Ou-Mandel effect in the x-ray regime and how to utilize the effect for the measurement of sub-attosecond time intervals and sub-angstrom optical path differences. The measurements are based on the detection of the variation of the dip in the coincidence count rate as a function of the parameters of the test sample. I have found that the dip can be observed for a broad range of parameters, and in particular it depends weakly on the number of layers of the multilayer mirrors and beam splitter. The relaxed requirements for stability and for coherence of the source suggest that the effect can be used for a large class of measurements for fundamental science and for a variety of applications. I also note that the approach I describe can be performed with present day x-ray sources although the expected count rate is quite moderate. New advanced sources such as the new high repetition rate free-electron lasers [49,50] are expected to enhance the count rate significantly. Consequently, my work opens the possibility for quantum precision measurements that are supported by the ultra-high spatio-temporal precision that is enabled by using quantum effects with x-rays.

6. Bibliography

- [1] C. K. Hong, Z. Y. Ou, and L. Mandel, *Phys. Rev. Lett.* **59**, 2044 (1987).
- [2] H. Lee, P. Kok, and J. P. Dowling, *J. Mod. Opt.* **49**, 2325 (2002).
- [3] P. Walther, J.-W. Pan, M. Aspelmeyer, R. Ursin, S. Gasparoni, and A. Zeilinger, *Nature* **429**, 158 (2004).
- [4] L. A. Rozema, J. D. Bateman, D. H. Mahler, R. Okamoto, A. Feizpour, A. Hayat, and A. M. Steinberg, *Phys. Rev. Lett.* **112**, 223602 (2014).
- [5] J.-H. Kim, T. Cai, C. J. K. Richardson, R. P. Leavitt, and E. Waks, *Optica* **3**, 577 (2016).
- [6] J. Rarity, P. Tapster, E. Jakeman, T. Larchuk, R. Campos, M. Teich, and B. Saleh, *Phys. Rev. Lett.* **65**, 1348 (1990).
- [7] J. Carolan *et al.*, *Science* **349**, 711 (2015).
- [8] R. B. Patel, A. J. Bennett, I. Farrer, C. A. Nicoll, D. A. Ritchie, and A. J. Shields, *Nat. Photonics* **4**, 632 (2010).
- [9] X. Ma, S. Zotter, J. Kofler, R. Ursin, T. Jennewein, Č. Brukner, and A. Zeilinger, *Nat. Phys.* **8**, 479 (2012).
- [10] C. Santori, D. Fattal, J. Vučković, G. S. Solomon, and Y. Yamamoto, *Nature* **419**, 594 (2002).
- [11] P. Kok, W. J. Munro, K. Nemoto, T. C. Ralph, J. P. Dowling, and G. J. Milburn, *Rev. Mod. Phys.* **79**, 135 (2007).
- [12] Z.-Y. J. Ou, *Multi-Photon Quantum Interference* (Springer US, New York, 2007).
- [13] Y. H. Shih and C. O. Alley, *Phys. Rev. Lett.* **61**, 2921 (1988).
- [14] J. Beugnon, M. P. A. Jones, J. Dingjan, B. Darquié, G. Messin, A. Browaeys, and P. Grangier, *Nature* **440**, 779 (2006).
- [15] J. S. Sidhu and P. Kok, *Phys. Rev. A* **95**, 063829 (2017).
- [16] J. P. Dowling, *Contemp. Phys.* **49**, 125 (2008).
- [17] D. Branning, A. L. Migdall, and A. V. Sergienko, *Phys. Rev. A* **62**, 063808 (2000).
- [18] E. Dauler, G. Jaeger, A. Muller, A. Migdall, and A. Sergienko, *J. Res. Natl. Inst. Stand. Technol.* **104**, 1 (1999).
- [19] A. Lyons, G. C. Knee, E. Bolduc, T. Roger, J. Leach, E. M. Gauger, and D. Faccio, *Sci. Adv.* **4**, eaap9416 (2018).
- [20] Y. Chen, M. Fink, F. Steinlechner, J. P. Torres, and R. Ursin, *Npj Quantum Inf.* **5**, 1 (2019).
- [21] B. W. Adams *et al.*, *J. Mod. Opt.* **60**, 2 (2013).

- [22] S. Shwartz, R. N. Coffee, J. M. Feldkamp, Y. Feng, J. B. Hastings, G. Y. Yin, and S. E. Harris, *Phys. Rev. Lett.* **109**, 013602 (2012).
- [23] R. Röhlberger, H. C. Wille, K. Schlage, and B. Sahoo, *Nature* **482**, 199 (2012).
- [24] R. Röhlberger, K. Schlage, B. Sahoo, S. Couet, and R. Ruffer, *Science* **328**, 1248 (2010).
- [25] F. Vagizov, V. Antonov, Y. V. Radeonychev, R. N. Shakhmuratov, and O. Kocharovskaya, *Nature* **508**, 80 (2014).
- [26] A. Schori, D. Borodin, K. Tamasaku, and S. Shwartz, *Phys. Rev. A* **97**, 063804 (2018).
- [27] S. Sofer, E. Strizhevsky, A. Schori, K. Tamasaku, and S. Shwartz, *Phys. Rev. X* **9**, 031033 (2019).
- [28] K. P. Heeg *et al.*, *Phys. Rev. Lett.* **111**, 073601 (2013).
- [29] S. Shwartz and S. E. Harris, *Phys. Rev. Lett.* **106**, 080501 (2011).
- [30] R. Schützhold, G. Schaller, and D. Habs, *Phys. Rev. Lett.* **100**, 091301 (2008).
- [31] A. Pálffy, C. H. Keitel, and J. Evers, *Phys. Rev. Lett.* **103**, 017401 (2009).
- [32] C. C. Gerry and P. L. Knight, *Introductory Quantum Optics* (Cambridge Univ. Press, Cambridge, 2004).
- [33] D. Borodin, A. Schori, F. Zontone, and S. Shwartz, *Phys. Rev. A* **94**, 013843 (2016).
- [34] A. F. Abouraddy, M. B. Nasr, B. E. A. Saleh, A. V. Sergienko, and M. C. Teich, *Phys. Rev. A* **65**, 053817 (2002).
- [35] M. B. Nasr, B. E. A. Saleh, A. V. Sergienko, and M. C. Teich, *Opt. Express* **12**, 1353 (2004).
- [36] D. Lopez-Mago and L. Novotny, *Opt. Lett.* **37**, 4077 (2012).
- [37] M. D. Mazurek, K. M. Schreiter, R. Prevedel, R. Kaltenbaek, and K. J. Resch, *Sci. Rep.* **3**, 1582 (2013).
- [38] D. Attwood, *Soft X-Rays and Extreme Ultraviolet Radiation: Principles and Applications* (Cambridge Univ. Press, Cambridge, 1999).
- [39] D. Spiga, *Development of Multilayer-Coated Mirrors for Future X-Ray Telescopes*, University of Milano-Bicocca, 2004.
- [40] I. Freund and B. F. Levine, *Phys. Rev. Lett.* **23**, 854 (1969).
- [41] P. Eisenberger and S. L. McCall, *Phys. Rev. Lett.* **26**, 684 (1971).
- [42] J. H. Underwood and T. W. Barbee, *Appl. Opt.* **20**, 3027 (1981).
- [43] B. E. A. Saleh and M. C. Teich, *Fundamentals of Photonics* (Wiley, New York, 2007).
- [44] R. J. Glauber, *Phys. Rev.* **130**, 2529 (1963).
- [45] The parameters are available online at: http://henke.lbl.gov/optical_constants/asf.html.

- [46] U. Bonse and M. Hart, *Appl. Phys. Lett.* **6**, 155 (1965).
- [47] P. Becker and U. Bonse, *J. Appl. Crystallogr.* **7**, 593 (1974).
- [48] K. Tamasaku, M. Yabashi, and T. Ishikawa, *Phys. Rev. Lett.* **88**, 044801 (2002).
- [49] S. Serkez, G. Geloni, S. Tomin, G. Feng, E. V. Gryzlova, A. N. Grum-Grzhimailo, and M. Meyer, *J. Opt.* **20**, 024005 (2018).
- [50] R. W. Schoenlein, S. Boutet, M. P. Minitti, and A. M. Dunne, *Appl. Sci.* **7**, 850 (2017).

תקציר

בעבודה זו אני מציג שיטת מטרולוגיה חדשה, המאפשרת למדוד פרקי זמן הקצרים מאטושנייה והפרשי מרחק אופטיים הקצרים מאנגסטרומ, באמצעות שימוש באפקט הונג-או-מנדל בתחום קרני ה-X. אני מציע תכנון מציאותי עבור מערכת אופטית אשר מדגימה את האפקט עם קרני X ומתאימה לטכנולוגיות הקיימות. זוהי ההתייחסות הראשונה לאפקט קוונטי זה והיא מהווה צעד חשוב בהרחבת האופטיקה הקוונטית לתחום קרני ה-X. יתר על כן, אני צופה כי התכנון שאני מתאר בעבודה זו יוביל לפיתוחם של יישומים חדשים רבים עבור מדע בסיסי ומחקר יישומי, ובמיוחד לשיטות מדידה קוונטיות בעלות דיוק גבוה מאוד באורכי גל של קרני X.

אפקט הונג-או-מנדל הינו אפקט קוונטי של התאבכות בין פונקציות הגל של שני פוטונים בלתי מובחנים, אשר נכנסים בו-זמנית לתוך שתי כניסות שונות של מפצל קרניים סימטרי. כתוצאה מהיותם בלתי מובחנים, הפוטונים תמיד מתגלים באותה היציאה של מפצל הקרניים, והמדידה של החפיפה בין הגילויים בשתי היציאות מתאפסת, מה שמהווה תוצאה שאיננה צפויה מבחינה קלאסית. כאשר הפרש הדרכים האופטיות בין הפוטונים גדל, הם אינם מגיעים יותר באותו הרגע אל מפצל הקרניים, ונעשים יותר ניתנים להבחנה. זה מעלה את ההסתברות לכך שתמיד חפיפה בין הגילויים בשתי היציאות, אשר מגיעה ל- $\frac{1}{2}$ כאשר הפוטונים נהיים מובחנים לחלוטין. בעקבות זאת, ההשהיה בין הפוטונים ניתנת למדידה בסקאלות זמן קצרות ביותר.

ההרחבה של אפקט הונג-או-מנדל לתחום קרני ה-X תפתח אפשרויות חדשות ומעניינות רבות לחקר הפיזיקה הקוונטית באמצעות שימוש ביתרונות הנובעים מהאנרגיה הגבוהה של פוטונים של קרני X. דוגמאות ליתרונות הללו הנם החודרניות של קרני ה-X יחסית לפוטונים אופטיים, היכולת לאפנן אותם לנשיאת מידע רב יותר והזמינות של גלאים המסוגלים למדוד את מספר הפוטונים הנמדדים, אשר מדגימים יעילויות גילוי גבוהות ורעש רקע זניח. היתרונות העיקריים של גישה זו לביצוע מדידות על פני שיטות עכשוויות הנם הדיוק הגבוה מאוד והדרישות הפחות מחמירות עבור היציבות של המערכת האופטית והקוהרנטיות של המקור. לפיכך, היא יכולה להתגבר על המכשולים העומדים בפני הטכנולוגיות העכשוויות ולאפשר לבצע מדידות של תופעות וגדלים פיזיקליים אשר מחוץ להישג ידן, והיא תהיה שימושית עבור מגוון רחב של דיסציפלינות מדעיות.

בכדי להדגים את האפקט, אני מתחיל בלכתנן את המערכת האופטית באופן סכמטי. המערכת המוצעת מורכבת ממקור ליצירת זוגות פוטונים בלתי מובחנים ורחבי-סרט בתדירות קרני X, המבוסס על תופעת המרת תדר פרמטרית ספונטנית, ומאינטרפרומטר רב-שכבתי, התואם לרוחב הסרט הרחב. אני ממשיך וממדל את הרכיבים האופטיים מבחינה מתמטית, לאחר מכן אני מחשב אנליטית את קצב החפיפה בין הגילויים במוצא המערכת, ולבסוף אני מבצע סימולציה של מערכת לדוגמה באמצעות Mathematica, עבור פרמטרים המתאימים למטרות התכנון ומשקפים מאפייני רכיבים מציאותיים. אני מוצא רוחב חצי מקסימום של כ-0.6 אטושניות בגרף של קצב החפיפה בין הגילויים כתלות בהשהיה בין הפוטונים. תוצאה זו ממחישה את היכולת של שיטת מטרולוגיה זו למדוד פרקי זמן הקצרים מאטושנייה והפרשי מרחק אופטיים הקצרים מאנגסטרומ.

עבודה זו נעשתה בהדרכתו של

פרופ' שרון שוורץ

מן המחלקה לפיסיקה של אוניברסיטת בר-אילן

אוניברסיטת בר-אילן

מטרולוגיית תת-אטושנייה

עם אפקט הונג-או-מנדל בקרני X

סרגיי וולקוביץ'

עבודה זו מוגשת כחלק מהדרישות לשם קבלת תואר מוסמך

במחלקה לפיסיקה של אוניברסיטת בר-אילן

